



1 **Global O<sub>3</sub>-CO Correlations in a Chemistry and Transport**  
2 **Model during July–August: Evaluation with TES Satellite**  
3 **Observations and Sensitivity to Input Meteorological Data**  
4 **and Emissions**

5

6 Hyun-Deok Choi<sup>1</sup>, Hongyu Liu<sup>1</sup>, James H. Crawford<sup>2</sup>, David B. Considine<sup>2,3</sup>, Dale J.  
7 Allen<sup>4</sup>, Bryan N. Duncan<sup>5</sup>, Larry W. Horowitz<sup>6</sup>, Jose M. Rodriguez<sup>5</sup>, Susan E. Strahan<sup>5,7</sup>,  
8 Lin Zhang<sup>8,9</sup>, Xiong Liu<sup>8</sup>, Megan R. Damon<sup>5,10</sup>, and Stephen D. Steenrod<sup>5,7</sup>

9

10 <sup>1</sup>National Institute of Aerospace, Hampton, VA

11 <sup>2</sup>NASA Langley Research Center, Hampton, VA

12 <sup>3</sup>Now at NASA Headquarters, Washington, D.C.

13 <sup>4</sup>University of Maryland, College Park, MD

14 <sup>5</sup>NASA Goddard Space Flight Center, Greenbelt, MD

15 <sup>6</sup>NOAA Geophysical Fluid Dynamics Laboratory, Princeton, NJ

16 <sup>7</sup>Universities Space Research Association, Columbia, MD

17 <sup>8</sup>Harvard University, Cambridge, MA

18 <sup>9</sup>Now at Peking University, Beijing, China

19 <sup>10</sup>Science Systems and Applications, Inc., Lanham, MD

20

21 **Submitted to *Atmos. Chem. Phys.*, 2016**

22

23 **Correspondence:**

24

25 Hongyu Liu

26 Chemistry and Dynamics Branch, Mail Stop 401B

27 NASA Langley Research Center, Hampton, VA 23681

28 Tel: 757-864-3191; Email: [Hongyu.Liu-1@nasa.gov](mailto:Hongyu.Liu-1@nasa.gov)

29



1 **Abstract.** We examine the capability of the Global Modeling Initiative (GMI) chemistry and  
2 transport model to reproduce global mid-tropospheric (618hPa) O<sub>3</sub>-CO correlations determined by  
3 the measurements from Tropospheric Emission Spectrometer (TES) aboard NASA's Aura satellite  
4 during boreal summer (July–August). The model is driven by three meteorological data sets  
5 (fvGCM with sea surface temperature for 1995, GEOS4-DAS for 2005, and MERRA for 2005),  
6 allowing us to examine the sensitivity of model O<sub>3</sub>-CO correlations to input meteorological data.  
7 Model simulations of radionuclide tracers (<sup>222</sup>Rn, <sup>210</sup>Pb, and <sup>7</sup>Be) are used to illustrate the  
8 differences in transport-related processes among the meteorological data sets. Simulated O<sub>3</sub> values  
9 are evaluated with climatological ozone profiles from ozonesonde measurements and satellite  
10 tropospheric O<sub>3</sub> columns. Despite the fact that the three simulations show significantly different  
11 global and regional distributions of O<sub>3</sub> and CO concentrations, all simulations show similar  
12 patterns of O<sub>3</sub>-CO correlations on a global scale. These patterns are consistent with those derived  
13 from TES observations, except in the tropical easterly biomass burning outflow regions.  
14 Discrepancies in regional O<sub>3</sub>-CO correlation patterns in the three simulations may be attributed to  
15 differences in convective transport, stratospheric influence, and subsidence, among other  
16 processes. To understand how various emissions drive global O<sub>3</sub>-CO correlation patterns, we  
17 examine the sensitivity of GMI/MERRA model-calculated O<sub>3</sub> and CO concentrations and their  
18 correlations to emission types (fossil fuel, biomass burning, biogenic, and lightning NO<sub>x</sub>  
19 emissions). Fossil fuel and biomass burning emissions are mainly responsible for the strong  
20 positive O<sub>3</sub>-CO correlations over continental outflow regions in both hemispheres. Biogenic  
21 emissions have a relatively smaller impact on O<sub>3</sub>-CO correlations than other emissions, but are  
22 largely responsible for the negative correlations over the tropical eastern Pacific, reflecting the fact  
23 that O<sub>3</sub> is consumed and CO generated during the atmospheric oxidation process of isoprene under



1 low  $\text{NO}_x$  conditions. We find that lightning  $\text{NO}_x$  emissions degrade both positive correlations at  
2 mid-/high- latitudes and negative correlations in the tropics because ozone production downwind  
3 of lightning  $\text{NO}_x$  emissions is not directly related to the emission and transport of CO. Our study  
4 concludes that  $\text{O}_3$ -CO correlations may be used effectively to constrain the sources of regional  
5 tropospheric  $\text{O}_3$  in global 3-D models, especially for those regions where convective transport of  
6 pollution plays an important role.

7

## 8 **1. Introduction**

9 Ozone ( $\text{O}_3$ ) is an important greenhouse gas in the troposphere and a pollutant at the surface.  
10 It is a primary source of the hydroxyl radical (OH), which controls the oxidizing power of the  
11 troposphere. Ozone in the troposphere is produced by photochemical oxidation of carbon  
12 monoxide (CO), methane, and volatile organic hydrocarbons (VOCs) in the presence of nitrogen  
13 oxides ( $\text{NO}_x \equiv \text{NO} + \text{NO}_2$ ). Its precursors are emitted by human activity (e.g., fossil fuel  
14 combustion and industrial processes), biomass burning, vegetation, soils, and lightning. Ozone is  
15 also transported down from the stratosphere by the Brewer Dobson circulation. Carbon monoxide  
16 is a product of incomplete combustion. Its sources include fossil fuel and biofuel combustion,  
17 biomass burning, and chemical production from atmospheric oxidation of methane, isoprene, and  
18 other VOCs. Its primary sink is reaction with OH.

19 Since CO is a precursor of tropospheric  $\text{O}_3$  and an excellent tracer for long-range transport  
20 of pollution owing to its tropospheric lifetime of a few months, correlations between  $\text{O}_3$  and CO  
21 are useful indicators of the efficiency of  $\text{O}_3$  production and export (e.g., Parrish et al., 1993; Mao  
22 and Talbot, 2004). Generally, a positive correlation in summer indicates strong photochemical



1 production of O<sub>3</sub> downwind of polluted regions (Chin et al., 1994; Tsutsumi and Matsueda, 2000).  
2 A negative correlation indicates stratospheric influence (Parrish et al., 1998; Hsu et al., 2004),  
3 photochemical O<sub>3</sub> destruction (Fishman and Seiler, 1983; Parrish et al., 1998; Mao and Talbot,  
4 2004), or chemical production of CO (Chin et al., 1994; Real et al., 2008). Small correlation  
5 coefficients and small linear regression slopes are indications of fresh pollution plumes that have  
6 not yet realized their O<sub>3</sub> production potential due to, for example, incomplete photochemical  
7 processes (Naja et al., 2003).

8 Many studies have used surface and/or aircraft observed O<sub>3</sub>-CO correlations to understand  
9 anthropogenic influences on O<sub>3</sub>, especially in the Northern Hemisphere (NH) continental outflow  
10 regions such as the northeastern US/northern Atlantic (Fishman and Seiler, 1983; Anderson et al.,  
11 1993; Parrish et al., 1993; Chin et al., 1994; Fehsenfeld et al., 1996; Parrish et al., 1998; Li et al.,  
12 2002; Honrath et al., 2004; Mao and Talbot, 2004) and the Asian Pacific Rim (Tsutsumi and  
13 Matsueda, 2000; Mauzerall et al., 2000). The studies found strong O<sub>3</sub>-CO correlations in outflow  
14 regions and concluded that the export of pollution from the NH major continents makes a  
15 significant contribution to total tropospheric O<sub>3</sub> over the NH during summer.

16 The observed O<sub>3</sub>-CO correlation coefficients and linear regression slopes have been used  
17 to evaluate the capability of models of chemistry and transport to produce proper O<sub>3</sub> levels from  
18 its precursors for the right reasons (e.g., Chin et al., 1994; Mauzerall et al., 2000; Zhang et al.,  
19 2006; Voulgarakis et al., 2011). Shim et al. (2009) examined the Mexico City pollution outflow  
20 using O<sub>3</sub>, CO, and their correlations from TES as well as aircraft measurements obtained during  
21 the Megacity Initiative: Local and Global Research Observations (MILAGRO) / Intercontinental  
22 Chemical Transport Experiment (INTEX-B) campaigns. These investigations found that TES data  
23 is characterized by smaller O<sub>3</sub>-CO correlation coefficients but larger linear regression slopes than



1 *in situ* observations at 618 hPa partly due to the lack of variability in TES CO. Two previous  
2 studies also examined TES global O<sub>3</sub>-CO correlations. Zhang et al. (2006) compared mid-  
3 tropospheric TES O<sub>3</sub>-CO correlations in July 2005 over the eastern United States with those from  
4 the GEOS-Chem model and International Consortium for Atmospheric Research on Transport and  
5 Transformation (ICARTT) aircraft observations (July 2004), finding that TES can provide good  
6 information on global mid-tropospheric O<sub>3</sub>-CO correlations. Voulgarakis et al. (2011) expanded  
7 the scope of Zhang et al. (2006), evaluating O<sub>3</sub>-CO correlations simulated by two independent  
8 models against five years of TES observations. They suggested that in addition to O<sub>3</sub>  
9 photochemical processes, transport may also play an important role in the O<sub>3</sub>-CO correlations.  
10 However, Voulgarakis et al. (2011) could not isolate the effect of transport because the two models  
11 in their study used different input meteorological data sets as well as different chemical and  
12 transport mechanisms.

13 In this paper, we present O<sub>3</sub> and CO simulations using the Global Modeling Initiative  
14 (GMI) chemistry and transport model (CTM) driven by three meteorological data sets. The model  
15 can incorporate different inputs and components (e.g., meteorological fields, emission inventories,  
16 and chemical mechanisms), allowing us to test the sensitivity of model simulations to input  
17 meteorological data sets (e.g., Douglass et al., 1999; Considine et al., 2005; Liu et al., 2016). Model  
18 simulations are evaluated using ozonesonde and satellite observations. We then test the model's  
19 capability to reproduce the mid-tropospheric O<sub>3</sub>-CO correlations determined from TES  
20 measurements. We present the differences in the simulated O<sub>3</sub>-CO correlations due to the use of  
21 different meteorological input data, and interpret those differences in terms of transport using  
22 radionuclide species (<sup>222</sup>Rn, <sup>210</sup>Pb, and <sup>7</sup>Be) as tracers of atmospheric transport (see Section 2.1.3).



1 We also investigate the effect of emission types on O<sub>3</sub> and CO concentrations and their correlations  
2 in the model.

3 This paper is organized as follows. Section 2: Descriptions of the GMI model,  
4 meteorological data sets, and observational data sets. Section 3: Presentation of the model  
5 simulations of radionuclides, O<sub>3</sub> and CO. Section 4: Evaluation of GMI O<sub>3</sub> and CO simulations  
6 with observations. Section 5: Evaluation of GMI O<sub>3</sub>-CO correlations with satellite observations  
7 from TES. Section 6: Analysis of the effects of various emission types on the model simulated O<sub>3</sub>-  
8 CO correlations. Section 7: Summary and conclusions.

9

## 10 **2. Model and Data**

### 11 **2.1. GMI**

#### 12 **2.1.1. The CTM**

13 The GMI CTM is a global 3-D composition model that combines both tropospheric and  
14 stratospheric chemical mechanisms, including 124 species, 322 chemical reactions, and 81  
15 photolysis reactions (Ziemke et al, 2006; Duncan et al., 2007a; Considine et al., 2008; Allen et al.,  
16 2010). The tropospheric mechanism includes a detailed description of tropospheric O<sub>3</sub>-NO<sub>x</sub>-  
17 hydrocarbon chemistry (Bey et al., 2001) with recent updates (e.g., see Allen et al., 2010). The  
18 stratospheric mechanism is described in Kinnison et al. (2001) and Douglass et al. (2004). The  
19 details of the GMI model are described in Duncan et al. (2007a) and Strahan et al. (2007). The  
20 basic structure of the model is described in Rotman et al. (2001).



1           The GMI model uses a flux-form semi-Lagrangian (FFSL) advection scheme (Lin and  
2 Rood, 1996) and also includes parameterizations of convection, wet scavenging, dry deposition,  
3 and planetary boundary layer mixing. The anthropogenic emission (e.g., fossil fuel emissions)  
4 scheme is from Bey et al. (2001), Benkovitz et al. (1996), and Duncan et al. (2007b). We use the  
5 anthropogenic emission inputs for 2005 for all simulations in this study. The biogenic emission  
6 scheme is calculated online based on Guenther et al. (2006) and biofuel emissions are estimated  
7 from the inventory and emission factors of Yevich and Logan (2003). Biomass burning emissions  
8 are from Duncan et al. (2003) climatology, where the spatial and seasonal variability are derived  
9 from satellite observations of monthly total fire counts. Lightning NO<sub>x</sub> emissions are calculated  
10 locally in deep convection events with the scheme of Allen et al. (2010) where flash rates are  
11 assumed to be proportional to the square of upward convective mass flux but constrained by  
12 monthly average climatological flash rates from V2.2 of the Optical Transient Detector and the  
13 Lightning Imaging Sensor (OTD/LIS) climatology. GMI uses modules developed at Harvard  
14 University to calculate wet scavenging (Mari et al., 2000; Liu et al., 2001) and dry deposition rates  
15 (Jacob and Wofsy, 1990).

16           Several studies have previously evaluated the GMI CTM simulations of tropospheric O<sub>3</sub>  
17 and CO. Ziemke et al. (2006) compared the tropospheric ozone columns (TOC) in an earlier  
18 version of the GMI CTM, which was driven by the fvGCM meteorological fields (details in Section  
19 2.1.2), with those determined from Ozone Monitoring Instrument/Microwave Limb Sounder  
20 (OMI/MLS) measurements from the NASA Aura satellite. The comparison showed similarities  
21 with respect to zonal and seasonal variations of TOC, but the model overestimated TOC over  
22 northern Africa by as much as 10 DU, likely due to desert dust effects while underestimating TOC  
23 over the western Pacific warm pool by up to 10 DU. Chandra et al. (2009) evaluated GMI TOC



1 when driven by the GEOS4 meteorological fields (see Section 2.1.2) with OMI/MLS TOC and  
2 found the model overestimated TOC by 5-10 DU for the latitude band 30°N - 35°N all the year  
3 and over east China in winter and spring when stratosphere-troposphere exchange (STE) is greatest.  
4 Duncan et al. (2008) showed that the annual average surface O<sub>3</sub> concentrations in the GMI/GEOS4  
5 simulation had a high bias of about 11%, with higher biases in summer when photochemical  
6 production is the dominant source of O<sub>3</sub>. Considine et al. (2008) examined the ability of  
7 GMI/fvGCM (4° × 5°) to represent the observed near-tropopause O<sub>3</sub> distributions and found that  
8 annual mean O<sub>3</sub> concentrations were biased high by 45% at the model thermal tropopause likely  
9 due to insufficient vertical resolution near the tropopause (~ 1.1 km) and/or too high vertical  
10 diffusivity.

11 For CO, Duncan et al. (2007a) compared GMI/fvGCM simulated tropospheric CO  
12 concentrations with NOAA Global Monitoring Division (GMD) surface observations. They  
13 showed that the model was biased low at most sites in local winter/spring likely due to  
14 overestimation of OH in the simulation when the CO burden is typically at an annual maximum.  
15 Schoeberl et al. (2006) showed that GMI/fvGCM was able to reproduce the upper  
16 troposphere/lower stratosphere (UT/LS) CO tape recorder caused by seasonal changes in biomass  
17 burning, as identified with the MLS data.

### 18 **2.1.2. fvGCM, GEOS4, and MERRA Meteorological Data Sets**

19 We drive the GMI CTM with three meteorological datasets from: the free-running NASA  
20 Global Modeling and Assimilation Office (GMAO) finite-volume General Circulation Model  
21 (fvGCM) for 1995, the Goddard Earth Observing System Data Assimilation System Version 4  
22 (GEOS4-DAS) for 2005, and the Modern-Era Retrospective Analysis for Research and



1 Applications (MERRA) for 2005. Note that the fvGCM is the general circulation model in the  
2 assimilation system used to generate GEOS4-DAS (Bloom et al., 2005). The native vertical  
3 coordinate of fvGCM and GEOS4-DAS models is a generalized hybrid sigma-pressure coordinate  
4 system with 55 vertical layers and a smooth transition between sigma in the troposphere (pressure  
5 > 200 hPa) and pure pressure in the stratosphere (top pressure 0.01 hPa). MERRA is a NASA  
6 atmospheric reanalysis data set from a new version of GEOS-DAS Version 5 (GEOS-5.2.0).  
7 GEOS-5 is a system of models integrated using the Earth System Modeling Framework (ESMF).  
8 Compared to GEOS-4, GEOS-5 adopts an analysis system developed jointly with the National  
9 Centers for Environmental Prediction (NCEP) and a different set of physics packages for the  
10 atmospheric GCM. MERRA has 72 vertical levels with a lid at 0.01 hPa (sigma-pressure  
11 coordinate interface at ~177 hPa). The native horizontal resolution of all meteorological data sets  
12 is  $1^\circ \times 1.25^\circ$ . To improve computational efficiency, we drive GMI CTM with the meteorological  
13 data sets at a degraded resolution ( $2^\circ$  latitude by  $2.5^\circ$  longitude).

14         The different convective parameterizations used to generate the meteorological data sets  
15 alters the characteristics of convective transport of chemical species. Both fvGCM and GEOS4  
16 use the deep convection scheme of Zhang and McFarlane (1995) and the shallow convection  
17 scheme of Hack (1994) whereas MERRA uses a modified version of the Relaxed Arakawa-  
18 Schubert scheme for convection (Moorthi and Suarez, 1992). **Figure 1** shows the latitude-pressure  
19 cross sections of zonal mean convective mass fluxes averaged over three meteorological data fields  
20 and the differences from the average during July – August. fvGCM shows the strongest shallow  
21 convection in the Southern Hemisphere (SH) mid- and low-latitudes among the models. GEOS4  
22 shows the strongest convection in the tropical middle troposphere. MERRA is characterized by  
23 the weakest shallow convection in both hemispheres. MERRA has the strongest tropical



1 convection in the lower free troposphere, but its tropical convection is not as deep as in the others.  
2 Shallow convection in fvGCM and GEOS4 extends to higher latitudes compared to MERRA.

### 3 **2.1.3. Radionuclide Tracers**

4 We conduct GMI model simulations of radionuclides ( $^{222}\text{Rn}$ ,  $^{210}\text{Pb}$ , and  $^7\text{Be}$ ) to examine  
5 the relative effects of convection, stratospheric influence, and large-scale subsidence on the  
6 transport of trace species and their sensitivity to input meteorological data sets.  $^{222}\text{Rn}$  has a half-  
7 life of 3.8 days and is emitted primarily from continental crust. It is useful as a tracer of convective  
8 transport in global models (e.g., Jacob et al., 1997).  $^{210}\text{Pb}$ , a decay daughter of  $^{222}\text{Rn}$ , has a  
9 radioactive half-life of 22.3 years, and  $^7\text{Be}$ , which is produced by cosmic ray spallation reactions  
10 in the stratosphere and UT, has a radioactive half-life of 53.3 days. Because  $^{210}\text{Pb}$  and  $^7\text{Be}$  attach  
11 to submicron aerosols after production and are therefore scavenged by precipitation or deposited  
12 to the surface, they have been used as a pair to test wet deposition schemes in global models (e.g.,  
13 Liu et al., 2001).  $^7\text{Be}$  is also used as a tracer for STE (Dibb et al., 1994; Liu et al., 2001; Liu et al.,  
14 2016). The ratio  $^7\text{Be}/^{210}\text{Pb}$  is useful as an indicator of vertical transport because the ratio is  
15 insensitive to precipitation scavenging (Koch et al., 1996).

## 16 **2.2. Data Sets**

### 17 **2.2.1. Ozonesonde $\text{O}_3$**

18 We use climatological ozone profiles from 23 ozonesonde stations averaged over July –  
19 August from 1985 to 2000, originally constructed by Considine et al. (2008) based on Logan (1999)  
20 and Thompson et al. (2003). The number of soundings at each station is adequate for defining  
21 monthly means used to evaluate the accuracy of the model results (Considine et al., 2008; Liu et  
22 al., 2016).



### 1    **2.2.2. Satellite Tropospheric Ozone Column (TOC)**

2            Three TOC products are used in this study: Total Ozone Mapping Spectrometer (TOMS)  
3    – Solar Backscatter Ultraviolet (SBUV), OMI-MLS, and directly retrieved TOC from TES. The  
4    TOMS-SBUV TOC and OMI-MLS TOC are determined using the tropospheric ozone residual  
5    (TOR) method, which involves subtracting measurements of SBUV and MLS stratospheric  
6    column ozone (SCO) from TOMS and OMI total column ozone, respectively (Fishman et al., 2003;  
7    Ziemke et al., 2006). The TES TOCs are integrated from directly retrieved volume mixing ratios.  
8    We did not consider different instrument sensitivities because integrating retrievals significantly  
9    reduces the error due to averaging over pressure ranges larger than TES vertical resolution  
10    (Osterman et al., 2008; Zhang et al., 2012). Tropopause pressure is taken from the GEOS4  
11    meteorological data ( $2^\circ \times 2.5^\circ$ ). A description of TES retrievals is given in Section 2.2.3.

### 12    **2.2.3. TES O<sub>3</sub> and CO.**

13            The TES instrument on EOS-Aura routinely provides observations of tropospheric O<sub>3</sub> and  
14    CO across the globe (Beer et al., 2001; Beer, 2006). The Aura satellite is on a polar sun-  
15    synchronous orbit with equator crossing at 01:45 (descending) and 13:45 (ascending) local time.  
16    TES is a Fourier transform infrared emission spectrometer with high spectral resolution ( $0.1 \text{ cm}^{-1}$ )  
17    and wide spectral range ( $650 - 3050 \text{ cm}^{-1}$ ) (Beer et al., 2001). The nadir footprint of TES is  $5 \times 8$   
18    km. TES observations consist of two modes: global survey and special observations (Beer et al.,  
19    2001). We use TES level 2, version 4 global survey nadir observations  
20    (<http://eosweb.larc.nasa.gov/>) and only O<sub>3</sub> and CO retrievals with the “Master” quality flag are  
21    used in this analysis. The retrievals of O<sub>3</sub> have 1 – 1.5 degrees of freedom (DOF) in the profile at  
22    mid-latitudes in summer, with peak sensitivities near 700 hPa and 300-400 hPa, respectively



1 (Parrington et al., 2008). TES CO profiles generally have 1 – 1.5 DOFs in the troposphere (Luo et  
2 al., 2007ab). Detailed descriptions of the TES instrument and the O<sub>3</sub> and CO retrieval algorithms  
3 are described in Beer et al. (2001, 2006), Worden et al. (2004), and Bowman et al. (2002, 2006).

4 In this study, we use O<sub>3</sub> and CO retrievals at 618 hPa level, where TES has good sensitivity  
5 for both O<sub>3</sub> and CO centered in the MT, and exclude latitudes > 60° where TES measurements are  
6 less reliable due to low brightness temperatures (Zhang et al., 2006). Due to limitation of TES  
7 vertical resolution (1 – 1.5 DOFs in the troposphere for both O<sub>3</sub> and CO), TES averaging kernels  
8 are applied to the simulations to take into account the different sensitivities of the instruments.  
9 TES uses MOZART model output binned by month and in blocks of 10° latitude by 60° longitude  
10 as a priori profiles (Worden et al., 2004). Validation of TES O<sub>3</sub> against ozonesondes showed that  
11 TES ozone typically has a high bias of about 10% in the UT (Worden et al., 2007) or 3-10 ppbv in  
12 the MT/UT (Nassar et al., 2008). TES CO has a negative bias (<10%) compared to aircraft  
13 measurements in the NH mid-latitude LT/MT during the INTEX-B mission (spring 2006) (Luo et  
14 al., 2007a).

15

### 16 **3. Model Simulations of Radionuclides, O<sub>3</sub>, and CO**

#### 17 **3.1. GMI Simulations of Radionuclides**

18 **Figures 2 and 3** show the latitude-pressure cross sections of zonal mean concentrations of  
19 <sup>222</sup>Rn and stratospheric fraction (%) of tropospheric <sup>7</sup>Be concentrations during July – August for  
20 the values averaged over three meteorological data sets and the differences from the mean.  
21 Differences in zonal mean <sup>222</sup>Rn concentrations at SH mid-latitudes among the three simulations  
22 are small despite much stronger shallow convection in fvGCM (**Figure 1**). This reflects the fact



1 that most convection at SH mid-latitudes occurs over the ocean. However, GMI/fvGCM  $^{222}\text{Rn}$   
2 concentrations in the UT at NH subtropics and mid-latitudes are  $\sim 20 - 70\%$  higher than those in  
3 other simulations due to the deeper convection in fvGCM (**Figure 1**). In the tropical UT/MT,  
4 GMI/MERRA produced the lowest  $^{222}\text{Rn}$  concentrations, consistent with the lower cutoff of  
5 convection in GMI/MERRA (**Figure 2**). This is not inconsistent with the largest stratospheric  
6 influence in the tropical UT/MT in GMI/MERRA among the three meteorological data sets  
7 (**Figure 3**). Previously, Liu et al. (2010) and Zhang et al. (2011) used GEOS-Chem simulations of  
8 CO and  $^{222}\text{Rn}$  (driven by GEOS4 DAS and GEOS5 DAS meteorological data) to show that the  
9 tropical convection in GEOS4 is deeper than in GEOS5. Because the MERRA reanalysis utilizes  
10 the same GCM as the GEOS5 DAS, it also utilizes the Relaxed Arakawa-Schubert (RAS)  
11 convection.

12 The stratospheric contribution to the lower-tropospheric  $^7\text{Be}$  concentrations in  
13 GMI/fvGCM peaks near  $30 - 75^\circ\text{N}$  ( $20 - 25\%$ ), in contrast to the GMI/GEOS4 and GMI/MERRA  
14 simulations (**Figure 3**). The GMI/GEOS4 and GMI/MERRA simulations show a similar pattern  
15 of stratospheric influence on the troposphere with maxima near  $0 - 30^\circ\text{S}$  and  $>30^\circ\text{S}$  ( $20 - 30\%$ ),  
16 respectively, in the LT. However, GMI/GEOS4 suggests more stratospheric influence than  
17 GMI/MERRA in the MT near  $30^\circ\text{S}$  ( $30 - 35\%$ ) and near  $30 - 45^\circ\text{N}$  ( $\sim 25\%$ ). The stratospheric  
18 impacts on the tropical MT/UT are weakest in GMI/fvGCM and strongest in GMI/MERRA. At  
19 NH mid-latitudes, stratospheric influences on the LT are largest and most extensive in  
20 GMI/fvGCM and smallest in GMI/MERRA. These differences in stratospheric influence that  
21 characterize these meteorological data sets will be used to interpret GMI  $\text{O}_3$  and CO simulations  
22 driven by these meteorological fields (Sections 3.2 and 4).

### 23 3.2. GMI Simulations of $\text{O}_3$ and CO



1           **Figures 4-5** show the latitude-pressure cross sections of zonal mean mixing ratios of O<sub>3</sub>  
2 and CO during July – August averaged over three simulations and the differences from the mean.  
3 The latitudinal distributions of O<sub>3</sub> from all simulations show lowest O<sub>3</sub> concentrations near the  
4 surface at high latitudes and in the tropical LT (**Figure 4**). Relatively low O<sub>3</sub> in the tropical free  
5 troposphere results from transport of ozone-poor air from the LT to UT/MT via deep convection.  
6 High O<sub>3</sub> concentrations are seen in the (subtropical) descending branches of the Hadley circulation  
7 partly due to the influence of STE. Compared with GMI GEOS4 and GMI/MERRA, GMI/fvGCM  
8 simulates higher O<sub>3</sub> in the NH mid-latitude MT and lower O<sub>3</sub> in the SH LT/MT. This is likely due  
9 to higher STE in the NH and weaker STE in the SH, respectively, as suggested by the higher (lower)  
10 fraction of stratospheric <sup>7</sup>Be seen in the GMI/fvGCM simulation compared to the other two  
11 simulations (**Figure 3**). On the other hand, GMI/MERRA simulates the highest O<sub>3</sub> in the tropical  
12 MT/UT as a result of “stronger but shallower” deep convection in the tropics (**Figure 1**). All  
13 simulations show the largest CO concentrations in the tropical LT/MT and NH mid-latitude  
14 boundary layer (**Figure 5**). The former reflects convective lifting of tropical biomass burning CO  
15 emissions and the latter anthropogenic CO emissions, respectively. Among the three simulations,  
16 GMI/fvGCM simulates the lowest CO concentrations in the tropical MT/UT as well as both  
17 hemispheres. In the NH MT/UT in GMI/fvGCM, the low CO concentrations result from high OH  
18 concentrations associated with high O<sub>3</sub> concentrations due to higher STE, which will be discussed  
19 in Section 4.1. In the SH GMI/fvGCM, the low CO concentrations are due to high OH  
20 concentrations as a result of too low NO<sub>x</sub> emissions from lightning (see Section 4.1). Tropical  
21 MT/UT CO concentrations in GMI/MERRA are not as high as those in GMI/GEOS4, again  
22 reflecting the “shallower” tropical deep convection in MERRA.

23



#### 1 4. Evaluation of GMI O<sub>3</sub> and CO Simulations with Observations

2 In this section, we evaluate GMI O<sub>3</sub> and CO simulations driven by the fvGCM, GEOS4,  
3 and MERRA meteorological data sets with ozonesonde O<sub>3</sub> vertical profiles, satellite TOC, and  
4 TES O<sub>3</sub> and CO retrievals.

##### 5 4.1. Ozone Vertical Profiles and Tropospheric Ozone Column

6 **Figure 6** compares GMI simulated tropospheric O<sub>3</sub> profiles with ozonesonde observations  
7 averaged over July-August for a range of latitudes. These results are typical of other stations at  
8 similar latitudes. GMI/fvGCM overestimates O<sub>3</sub> in the NH high-/mid-latitude UT/MT (e.g.,  
9 Churchil, Hohenpeissenberg, and Sapporo). This may be due to excessive STE given the relatively  
10 high fractions of <sup>7</sup>Be from the stratosphere (**Figure 3**). The overestimate may also be partly  
11 attributed to strong convective mass fluxes in the NH mid-latitude that lift more O<sub>3</sub> and/or its  
12 precursors from the surface (**Figures 1-2**). **Figure 6** also shows that GMI/fvGCM underestimates  
13 O<sub>3</sub> in the SH (e.g., Reunion Island). Since stratospheric <sup>7</sup>Be fractions are relatively low in this  
14 simulation, the O<sub>3</sub> underestimate may be due to overly weak STE (cf. **Figure 3**). Low emissions  
15 of lightning NO<sub>x</sub>, an important precursor of tropospheric O<sub>3</sub> could also play a role. Lightning NO<sub>x</sub>  
16 emissions between 10°S and 70°S in GMI/fvGCM during July-August are similar to those in  
17 GMI/GEOS4 and GMI/MERRA, but the emissions during May-June are a factor of ~ 2.5 lower  
18 than those in GMI/GEOS4 and GMI/MERRA (**Table 1**). Since O<sub>3</sub> has a lifetime of weeks to  
19 months in the UT/MT, a low-O<sub>3</sub> bias during May-June will lead to lower O<sub>3</sub> during July-August  
20 in GMI/fvGCM. GMI/GEOS4 simulates O<sub>3</sub> in both hemispheres reasonably well but  
21 underestimates O<sub>3</sub> in the tropical UT/MT, as seen at Paramaribo and Nairobi in **Figure 6**.  
22 GMI/MERRA underestimates O<sub>3</sub> in the NH high-latitude UT (e.g., Resolute) likely due to weak



1 STE compared to GMI/GEOS4 as suggested by  $^7\text{Be}$  tracer simulations (**Figure 3**), while it  
2 overestimates  $\text{O}_3$  with a high bias in the SH subtropics (e.g., Samoa and Reunion Island) because  
3 of a combination of excessive influences from lightning  $\text{NO}_x$  emissions in May (**Table 1**) and STE  
4 (or subsidence from UT) (**Figure 3**). In addition, the shallower tropical convection (**Figure 1**)  
5 accompanied by larger STE contribution in the southern tropical MT/UT (**Figure 3**) results in less  
6 clean air being lifted from the LT to MT/UT.

7 **Figure 7** shows GMI simulated zonal mean TOCs averaged over July – August in  
8 comparison with TORs determined from TOMS/SBUV (Fishman et al., 2003), OMI/MLS  
9 (Ziemke et al., 2006), and TOCs directly retrieved from TES measurements. The World  
10 Meteorological Organization (WMO) definition of thermal tropopause is used to calculate the  
11 model TOC, following Liu et al. (2016). The latitudinal distribution of TOCs shows a trough in  
12 the tropics and polar regions, and a peak at mid-latitudes in both the models and the observations.  
13 The TORs determined from TOMS/SBUV and OMI/MLS agree well with each other in the NH,  
14 but those from OMI/MLS are lower at  $\sim 10^\circ\text{N}$  and higher at south of  $50^\circ\text{S}$ . The TOCs determined  
15 from TES are more similar to the OMI/MLS TORs, but biased high in the northern subtropics, and  
16 biased low at south of  $40^\circ\text{S}$ . A comparison of **Figure 7** with **Figure 6** indicates that the TOCs from  
17 three model simulations coincide with the above results from model evaluations with ozonesonde  
18  $\text{O}_3$  profiles. For example, both evaluations suggest negative biases in the SH and positive biases  
19 in the NH high-/mid-latitudes in GMI/fvGCM, and positive biases in the southern subtropics in  
20 GMI/MERRA.

## 21 4.2. $\text{O}_3$ and CO Concentrations at 618 hPa



1           **Figure 8** shows the July-August mean concentrations of O<sub>3</sub> and CO at 618 hPa in the GMI  
2 simulations. **Figure 9** shows the corresponding global distributions of <sup>222</sup>Rn concentrations,  
3 stratospheric fractions (%) of mean tropospheric <sup>7</sup>Be concentrations, and ratios <sup>7</sup>Be/<sup>210</sup>Pb. All  
4 simulations show highest O<sub>3</sub> concentrations at NH mid-latitudes and lowest O<sub>3</sub> concentrations in  
5 the tropical western Pacific. They also simulate a narrow band of relatively high O<sub>3</sub> concentrations  
6 in the southern tropics and subtropics. GMI/fvGCM simulates highest O<sub>3</sub> concentrations at NH  
7 mid/high latitudes (**Figure 8**, left panel) likely due to STE, as indicated by a large fraction of <sup>7</sup>Be  
8 transported down from the stratosphere (**Figure 9**, middle top panel). By contrast, it simulates the  
9 lowest O<sub>3</sub> concentrations in the southern tropics and subtropics, especially over southern Africa  
10 and South Atlantic Ocean. In this region, GMI/MERRA simulates the highest O<sub>3</sub> concentrations  
11 attributed to high lightning NO<sub>x</sub> emissions (**Table 1**), large STE (**Figure 9**, middle bottom panel),  
12 and biomass burning emissions lifted by shallow but strong convection (Section 3; **Figure 9**, left  
13 bottom panel). Thompson et al. (1996) previously suggested that O<sub>3</sub> maximum observed in  
14 southern Africa and the adjacent Atlantic during September - October 1992 is caused by the  
15 coincidence of O<sub>3</sub> precursors from biomass burning with long residence time, and deep convection  
16 with additional lightning NO<sub>x</sub> and biogenic sources. As we will show in Section 5, the emission  
17 types contributing to the O<sub>3</sub> enhancements over this region in July – August mainly include  
18 lightning NO<sub>x</sub> and, to a lesser extent, biomass burning.

19           All simulations show a similar pattern of CO concentrations at 618 hPa, e.g., CO  
20 enhancements due to biomass burning emissions lifted by convection (e.g., South America, Africa,  
21 Indonesia, and Alaska) and anthropogenic emissions (e.g., East Asia, South Asia, and eastern  
22 North America) (**Figure 8**, right column). This pattern also reflects the geographic distribution of  
23 these emissions. GMI/fvGCM simulates lowest CO concentrations at 618 hPa in most of the



1 polluted regions due to stronger STE of O<sub>3</sub>, as discussed in Section 4.1. GMI/GEOS4 simulates  
2 slightly lower CO concentrations in East and South Asia, North America and their outflow regions,  
3 and Indonesia than GMI/MERRA does. GMI/GEOS4 also simulates lower CO concentrations over  
4 subtropical South American and African westerly outflow regions.

5 To evaluate GMI O<sub>3</sub> and CO simulations with satellite observations, we use TES retrievals  
6 at 618 hPa where TES has good sensitivity for both O<sub>3</sub> and CO in the MT (Zhang et al., 2006).  
7 GMI model output was sampled along the TES orbit track at the observation time and then  
8 interpolated onto the 67 vertical pressure levels of TES retrievals. Since the model output was  
9 saved every 3 hours, the temporal offset with TES is up to 1.5 hours. To compare the model output  
10 with the TES retrieved profiles, TES averaging kernels and *a priori* were applied to the model  
11 output. Both the model output and TES data were gridded onto grids of 10° latitude by 10°  
12 longitude by averaging all values within each grid box. **Figures 10-11** show the mean  
13 concentrations of O<sub>3</sub> and CO at 618 hPa observed by TES during July - August 2005 and  
14 corresponding GMI CTM results.

15 TES observed enhanced O<sub>3</sub> concentrations over the Middle East, northern Africa, southern  
16 Africa, North America, and East Asia (**Figure 10**). Increased levels of O<sub>3</sub> were also observed in  
17 continental outflow regions, especially the northwestern Pacific, North Atlantic, tropical south  
18 Atlantic, and southern subtropical Indian Ocean. All simulations capture the spatial distributions  
19 of O<sub>3</sub> well but underestimate the enhancements over southern Africa and adjacent oceans.  
20 GMI/fvGCM simulates reasonably well the TES-observed O<sub>3</sub> enhancements at NH mid/high  
21 latitudes but slightly underestimates the low O<sub>3</sub> concentrations in the tropical western Pacific and  
22 Indian Ocean. GMI/GEOS4 and GMI/MERRA simulations show lower O<sub>3</sub> concentrations at NH  
23 mid/high latitudes compared to TES observations. However, considering that TES O<sub>3</sub> has a



1 positive bias of 3-10 ppbv in the MT (Nassar et al., 2008), GMI/fvGCM may very well  
2 overestimate O<sub>3</sub> at NH mid-latitudes while GMI/GEOS4 and GMI/MERRA simulations are closer  
3 to reality. This conclusion is consistent with that from the comparison of GMI simulations with  
4 ozonesonde observations (**Figure 6**).

5 Enhanced CO concentrations were observed by TES over Africa, South America, North  
6 America, and Eurasia (**Figure 11**). All simulations underestimated CO concentrations in most of  
7 those CO hot spots in the NH. GMI/GEOS4 captured fairly well high CO concentrations over  
8 biomass burning regions in South America and Africa. However, considering TES CO biases, i.e.,  
9 a negative bias at NH mid-latitudes and a positive bias in the tropics (Luo et al., 2007a; Lopez et  
10 al., 2008), all simulations significantly underestimate CO enhancements at NH mid-latitudes but  
11 simulate better CO enhancements over the tropical biomass burning regions. This is consistent  
12 with a previous study by Shindell et al. (2006) who found multi-model underestimate of NH  
13 extratropical CO likely due to current inventories underestimating fossil fuel emissions in East  
14 Asia and biomass burning emissions in south-central Africa.

15

## 16 **5. O<sub>3</sub> and CO Relationships**

17 In this section, we examine O<sub>3</sub> and CO relationships at 618hPa in GMI CTM. We interpret  
18 GMI simulated O<sub>3</sub>-CO correlations and their slopes in the context of emissions, photochemical  
19 transformation, and transport (e.g., convection, STE, and large-scale subsidence), using model  
20 meteorological data and radionuclide simulations. We then evaluate them with those derived from  
21 TES satellite observations.

### 22 **5.1. GMI O<sub>3</sub>-CO Correlations**



1           **Figure 12** shows the  $O_3$ -CO correlation coefficients (R) and linear regression slopes  
2   ( $dO_3/dCO$ ) at 618 hPa for July – August, as calculated using the reduced major axis method with  
3   3-hourly output from the GMI/fvGCM, GMI/GEOS4, and GMI/MERRA simulations. We discuss  
4   the common features in the correlation patterns in all simulations, followed by their discrepancies.  
5   All simulations show strong positive  $O_3$ -CO correlations and large  $dO_3/dCO$  enhancement ratios  
6   in the NH major continental outflow regions, e.g., Atlantic Seaboard, northern Atlantic, and  
7   northern Pacific, consistent with previous modeling studies (Zhang et al., 2006; Voulgarakis et al.,  
8   2011) and in situ observations (e.g., Anderson et al. 1993; Chin et al., 1994; Jaffe et al., 1996;  
9   Parrish et al., 1998; Tsutsumi and Matsueda, 2000; Mao and Talbot, 2004). Our simulations also  
10   suggest a much larger area with high correlations that extends from the NW to NE Pacific. We  
11   found that strong positive correlation regions are not co-located with maximum  $O_3$  and CO  
12   concentrations in all simulations. Instead, they are located between most polluted and clean areas,  
13   reflecting the intrusion of high  $O_3$  (and CO) air from mid-latitudes and low  $O_3$  (and CO) air from  
14   the tropics. Fishman and Seiler (1983) and Mauzerall et al. (2000) previously suggested that strong  
15   positive  $O_3$ -CO correlations in low CO regions may be caused by the depletion of both  $O_3$  and CO  
16   in tropical air.

17           All simulations show positive  $O_3$ -CO correlations in the SH marine regions, but  
18   GMI/MERRA simulates much stronger negative correlations over the equatorial Atlantic. The  
19   latter reflects the stronger convection in the LT/MT in MERRA, which will be discussed below.  
20   Positive  $O_3$ -CO correlations were previously observed over the tropical South Atlantic during the  
21   TRACE-A aircraft mission (September–October, 1992) (e.g., Collins et al., 1996). Collins et al.  
22   concluded that the  $O_3$ -CO correlations over the tropical South Atlantic are more affected by in situ



1 photochemical production from aged biomass burning plumes (positive O<sub>3</sub>-CO correlation) than  
2 transport from the stratosphere (negative O<sub>3</sub>-CO and O<sub>3</sub> - dew point correlations).

3 Strong positive O<sub>3</sub>-CO correlations are present in all simulations at 618 hPa over Indonesia  
4 (**Figure 12**), reflecting convective transport of biomass burning CO (**Figure 8**) and photochemical  
5 production of O<sub>3</sub> from its precursors. The dO<sub>3</sub>/dCO enhancement ratios over Indonesia are not as  
6 large as those over the NH mid-latitude continental outflow regions due to the fact that biomass  
7 burning emits NO<sub>x</sub> less efficiently than fossil fuel does.

8 Positive O<sub>3</sub>-CO correlations over the westerly African biomass burning outflow region  
9 (southern Indian Ocean, ~ 45°S) are seen in all simulations (**Figure 12**). The positive O<sub>3</sub>-CO  
10 correlations over both the NH mid-latitude continental outflow regions and the westerly African  
11 biomass burning outflow regions mainly reflect O<sub>3</sub> and CO signatures from different sources: 1)  
12 anthropogenic emissions of CO and other O<sub>3</sub> precursors in the former and biomass burning  
13 emissions in the latter (**Figure 8**), and 2) significant influences from the stratosphere and  
14 subsidence from UT/LS (**Figure 9**, middle and right columns, respectively). In the case of 1), the  
15 dO<sub>3</sub>/dCO slopes in the westerly African biomass burning outflow are smaller than those in the NH  
16 mid-latitude continental outflow, again reflecting the lower efficiency of biomass burning NO<sub>x</sub>  
17 emissions than that of fossil fuel NO<sub>x</sub> emissions. In the case of 2), mixing of stratospheric air (high  
18 O<sub>3</sub>) with polluted air masses (high CO) has previously been found associated with positive O<sub>3</sub>-CO  
19 correlations downwind from outflow regions (Cooper et al., 2002; Kim et al., 2013).

20 Strong negative O<sub>3</sub>-CO correlations are seen in all simulations over the northern tropical  
21 eastern Pacific, Caribbean, northern tropical Atlantic, and equatorial Africa. These negative  
22 correlations are primarily a result of convective transport of low-O<sub>3</sub> air masses impacted by



1 biogenic emissions. As will be discussed in Section 6, significant decreases in O<sub>3</sub> and increases in  
2 CO occur near the above regions due to atmospheric oxidation of biogenic VOCs (e.g., isoprene)  
3 over tropical America and Africa. In addition, our results show weak positive (in GMI/fvGCM  
4 and GMI/GEOS4) or strong negative (in GMI/MERRA) O<sub>3</sub>-CO correlations over much of the  
5 southern tropics and subtropics, especially near the biomass burning outflow regions. Negative  
6 O<sub>3</sub>-CO correlations in the southern tropics during July-August were previously reported by  
7 Fishman and Seiler (1983). Based on aircraft measurements, they concluded that O<sub>3</sub> destruction in  
8 the southern tropical LT, where the major CO sources (biomass burning emissions) are located,  
9 may lead to strong negative correlations (see their Figure 3).

10 All GMI simulations show strong negative O<sub>3</sub>-CO correlations over the Asian continent  
11 including the Middle East (**Figure 12**). Over Southwest China (e.g., Sichuan Basin), monsoonal  
12 convective lifting of air masses with high-CO and low-O<sub>3</sub> leads to negative O<sub>3</sub>-CO correlations.  
13 For most of other regions, high O<sub>3</sub> and low CO associated with stratospherically influenced air  
14 (**Figure 9**, middle column) result in negative O<sub>3</sub>-CO correlations with large (negative) dO<sub>3</sub>/dCO  
15 ratios. As will be discussed in Section 6, lightning NO<sub>x</sub> emissions also contribute to these negative  
16 correlations over the Asian continent. Our simulations over the Tibetan Plateau are consistent with  
17 the study of Wang et al., (2006), who inferred negative O<sub>3</sub>-CO correlations from in situ  
18 measurements at Mount Waliguan located at the northeastern edge of the Tibetan Plateau during  
19 summer due to downward transport from the UT/LS.

20 While the O<sub>3</sub>-CO correlations in the three simulations show similarities, they also show  
21 differences. The global O<sub>3</sub>-CO correlation patterns in GMI/fvGCM and GMI/GEOS4 are more  
22 similar, presumably because fvGCM is the GCM in the GEOS4 assimilation and they use the same  
23 convection scheme. Even so, significantly different O<sub>3</sub>-CO correlation coefficients between



1 GMI/fvGCM and GMI/GEOS4 are seen in northern Africa, where the former simulates strong  
2 negative but the latter shows weak positive correlations. As indicated by radionuclide tracers ( $^{210}\text{Pb}$   
3 and  $^7\text{Be}$ ), fvGCM has relatively stronger large-scale subsidence over northern Africa at 618 hPa  
4 than GEOS4, resulting in strong correlations with a large negative slope. In addition, the  $\text{O}_3\text{-CO}$   
5 correlations in GMI/MERRA are strongly negative over northern South America, tropical western  
6 South Atlantic Ocean, Indian Ocean, and tropical western Pacific Ocean. By contrast, the  
7 correlations in these regions in GMI/fvGCM and GMI/GEOS4 are either weak or positive. The  
8 convection in fvGCM is much weaker than in GEOS4 or MERRA except at SH mid-latitudes and  
9 over Tibetan Plateau (not shown). MERRA has the strongest convection in Central America,  
10 tropical western Pacific Ocean, tropical eastern Pacific Ocean, tropical western Atlantic Ocean,  
11 tropical eastern Indian Ocean, and Bay of Bengal. These differences of convective mass fluxes  
12 result in broader regions with negative  $\text{O}_3\text{-CO}$  correlations in the tropics in GMI/MERRA than  
13 those in GMI/fvGCM and GMI/GEOS4. Kim et al. (2013) also simulated different  $\text{O}_3\text{-CO}$   
14 correlations in some tropical regions with GEOS-Chem driven by GEOS4 and GEOS5  
15 meteorological data sets because of the model transport error associated with deep convection.

## 16 **5.2. Evaluation of GMI $\text{O}_3\text{-CO}$ Correlations with TES Observations**

17 **Figures 13** and **14** show the  $\text{O}_3\text{-CO}$  correlation coefficients ( $R$ ) and linear regression slopes  
18 ( $d\text{O}_3/d\text{CO}$ ), respectively, at 618 hPa as determined by TES observations for July - August 2005,  
19 and corresponding GMI CTM results with 3-hourly output sampled along the TES orbit tracks.  
20 Values are calculated in  $10^\circ \times 10^\circ$  grid cells. The regions of  $> 60^\circ\text{S}$  and  $> 60^\circ\text{N}$  are excluded in this  
21 study because  $\text{O}_3$  and  $\text{CO}$  concentrations over these regions are low (**Figure 8**) and absolute co-  
22 variances of  $\text{O}_3$  and  $\text{CO}$  over these regions are also low (not shown). Therefore, as suggested by  
23 Voulgarakis et al. (2011), discrepancies in these regions are not scientifically important in terms



1 of the O<sub>3</sub>-CO correlation. Since only two months of TES O<sub>3</sub> and CO observations were used, the  
2 correlation patterns are somewhat patchy and correlations are weak ( $|R| < 0.2$ ) over more than half  
3 of the globe. Using TES data for July – August over 5 years improves the consistency of the  
4 correlation patterns (**Figure 15**), as discussed later. TES-observed O<sub>3</sub> and CO concentrations show  
5 highest correlations (R up to 0.6) with large slopes over the western Pacific, and relatively high  
6 correlations (R = 0.2-0.4) with relatively large slopes over North America, the Middle East,  
7 northern South America, central and southern Africa, as well as continental outflow regions, e.g.,  
8 northwestern Pacific Ocean, western Indian Ocean, subtropical South Atlantic Ocean, tropical  
9 eastern Pacific, and northwestern Atlantic (**Figures 13** and **14**). Negative correlations were  
10 observed over the Tibetan Plateau (R < -0.6), northern Africa, and SH mid-latitudes (R < -0.4)  
11 (**Figure 13**). Global TES O<sub>3</sub>-CO correlation patterns and magnitudes are similar to those reported  
12 by Zhang et al. (2006) and Voulgarakis et al. (2011). The slope patterns (**Figure 14**) follow the  
13 correlation ones (**Figure 13**), suggesting that the slopes of the regression lines are useful indicators  
14 of the correlation strength.

15 The GMI simulated O<sub>3</sub>-CO correlation coefficients and linear regression slopes (dO<sub>3</sub>/dCO)  
16 calculated from each of the three model outputs sampled along the TES orbit tracks show similar  
17 global patterns but overall weaker correlations (**Figure 13**) and smaller slopes (**Figure 14**) than  
18 non-sampled raw model results (**Figure 12**) due to spatiotemporal sampling and application of  
19 TES averaging kernels. All simulations capture the TES-observed positive O<sub>3</sub>-CO correlations in  
20 various regions. On the other hand, all simulations indicate strong negative correlations over the  
21 Tibetan Plateau and tropical convective regions where TES misses such correlations or only shows  
22 much weaker negative correlations in much narrower areas.



1 To get a more statistically robust view of TES O<sub>3</sub>-CO correlations, we conduct a similar  
2 analysis using multi-year observations. **Figure 15** shows the O<sub>3</sub>-CO correlation coefficients (R)  
3 and linear regression slopes (dO<sub>3</sub>/dCO) at 618 hPa as determined by TES O<sub>3</sub> and CO retrievals for  
4 July - August over 5 years (2005 – 2009). Values are calculated in 4°x5° grid cells. The global  
5 distributions provide more details and are consistent with the coarse patterns for July – August  
6 2005 shown in **Figures 13** and **14**. The negative correlations over the Tibetan Plateau and northern  
7 Africa are more apparent than those using the TES data only for July – August 2005 (**Figure 13**).  
8 Overall our results of multi-year (2005 – 2009) O<sub>3</sub>-CO correlation coefficients at 618 hPa for July  
9 – August are similar to those inferred from the mean mid-tropospheric (400 – 800 hPa) TES O<sub>3</sub>  
10 and CO concentrations averaged over July – August 2005 – 2008 (Voulgarakis et al., 2011).

11

## 12 **6. Sensitivity of O<sub>3</sub>-CO Correlations to Emissions**

13 In order to understand how O<sub>3</sub>-CO correlation patterns are driven by emissions, we  
14 examine the sensitivity of O<sub>3</sub>-CO correlations to emission types in the GMI model driven by the  
15 MERRA meteorological fields, which represent the state-of-the-art of GEOS-DAS at the time of  
16 this study. **Figures 16 - 19** show the mean changes in O<sub>3</sub> and CO concentrations (ppbv) and their  
17 correlation coefficients, as well as the areas where correlation signs change relative to the standard  
18 simulation at 618 hPa when each emission type (fossil fuel, biomass burning, biogenic, and  
19 lightning NO<sub>x</sub> emissions) is excluded in the model for July – August 2005. **Figure 20** shows the  
20 O<sub>3</sub>-CO correlation coefficients (R) at 618 hPa in the standard simulation and when each emission  
21 type is excluded. Results are calculated using 3-hourly model output. These figures provide the  
22 context for discussions in this section.



1 Fossil fuel emissions substantially increase  $O_3$  (by ~5-20 ppbv) and CO (by ~10-30 ppbv)  
2 in the NH, notably over the Asian and North American continental outflow regions (**Figure 16ab**).  
3 Fossil fuel emissions lead to strengthened  $O_3$ -CO correlations with correlation signs changing from  
4 negative to positive over the Asian and North American outflow regions (**Figures 16cd** and **20b**).  
5 Such effects are also seen over Europe, the Arabian Sea, the northern Bay of Bengal, and the  
6 northeastern Pacific (**Figure 16cd**). Fossil fuel emissions result in stronger negative  $O_3$ -CO  
7 correlations over part of the Asian continent (**Figure 16c**). This is especially true over the Tibetan  
8 Plateau where low-level convergence transports air masses with low- $O_3$  and high-CO to the middle  
9 troposphere.

10 Biomass burning emissions increase  $O_3$  (by ~2-10 ppbv) and CO (by > 25ppbv) in the  
11 easterly outflow in the tropical South America and Central Africa, in the westerly outflow in the  
12 southern subtropics, and over Indonesia (**Figure 17ab**). They are responsible for the positive  
13 correlations in the SH mid- and high- latitudes (**Figures 17cd** and **19c**). Without biomass burning  
14 emissions,  $O_3$ -CO correlations over the westerly outflow in the southern subtropics and most of  
15 the SH mid- and high- latitudes would be negative or very weak (**Figures 17c** and **20c**). By contrast,  
16 biomass burning emissions degrade an already strong correlation from fossil fuel emissions in the  
17 NH (e.g., over part of the tropical western Pacific, Bay of Bengal, NH subtropical Atlantic, and  
18 especially NH high latitudes, **Figure 17d**). In the tropics, biomass burning emissions strengthen  
19 the positive correlations in Indonesia and weaken the negative correlations over the tropical South  
20 American outflow region. In the two models of Voulgarakis et al. (2011), biomass burning  
21 emissions have the largest impact on the  $O_3$ -CO correlations in the tropics, especially downwind  
22 of Central Africa and South America where biomass burning emissions changed the correlation  
23 sign from negative to positive. Our results show no apparent changes in the  $O_3$ -CO correlation



1 signs (negative) in these downwind regions. This may reflect the differences in biomass burning  
2 emissions and/or chemical mechanisms used in the two studies.

3 Biogenic emissions increase O<sub>3</sub> concentrations at 618 hPa by ~ 2-6 ppbv in the NH  
4 subtropics and mid-latitudes, but decrease O<sub>3</sub> concentrations by up to ~10 ppbv in tropical South  
5 America, tropical Africa, and Indonesia (**Figure 18a**). The latter mainly reflects the fact that O<sub>3</sub> is  
6 consumed during the atmospheric oxidation process of isoprene under low NO<sub>x</sub> conditions (Fan  
7 and Zhang, 2004; Seinfeld and Pandis, 1998). Biogenic emissions have large positive impacts on  
8 CO concentrations in the easterly and westerly outflow regions of South America and Africa, in  
9 the North American outflow, over Southwest China and Indonesia, as well as in the SH background  
10 (**Figure 18b**). The O<sub>3</sub>-CO correlations in the model show smaller sensitivity to biogenic emissions  
11 relative to other emission types (**Figures 18c** and **20d**). Nevertheless, biogenic emissions lead to  
12 strong negative O<sub>3</sub>-CO correlations over the tropical eastern Pacific Ocean due to reduced O<sub>3</sub> and  
13 enhanced CO concentrations associated with these emissions (**Figures 18cd** and **20d**). Such effects  
14 are also seen over central Africa, easterly South American outflow, westerly South American  
15 outflow, Indonesia, and subtropical western Pacific.

16 Lightning NO<sub>x</sub> emissions increase O<sub>3</sub> concentrations at 618 hPa by up to ~15-25 ppbv at  
17 NH subtropics and mid-latitudes, and by up to ~15-30 ppbv at SH tropics and subtropics (**Figure**  
18 **19a**). Such increases are relatively larger in those regions with subsiding air from the UT (cf.,  
19 **Figure 9**, right bottom panel), where the largest effect of lightning NO<sub>x</sub> emissions occurs. The  
20 resulting increase in OH concentrations leads to a general decrease in CO concentrations with  
21 maximum effects in the tropics and SH subtropics (**Figure 19ab**). Consequently, lightning NO<sub>x</sub>  
22 emissions weaken both the positive O<sub>3</sub>-CO correlations at mid- and high- latitudes and the negative  
23 correlations in the tropics (**Figures 19cd** and **20e**). They alter the correlation signs from positive



1 to negative in various areas where the correlations are generally weak (**Figure 19d**). Our results  
2 are in contrast with those of Voulgarakis et al. (2011) who showed that lightning NO<sub>x</sub> emissions  
3 appeared to increase the O<sub>3</sub>-CO correlations (400-800 hPa) in various regions (e.g., tropical eastern  
4 Pacific, NH continental outflow regions). These may partly reflect the differences in the altitude  
5 and strength of lightning NO<sub>x</sub> emissions.

6

## 7 **7. Summary and Conclusions**

8 We have examined the capability of the Global Modeling Initiative (GMI) chemistry and  
9 transport model (CTM) to reproduce the global mid-tropospheric O<sub>3</sub>-CO correlations from the TES  
10 instrument onboard the NASA Aura satellite during boreal summer (July – August). The model  
11 was driven by three meteorological data sets (fvGCM for 1995, GEOS4 for 2005, MERRA for  
12 2005), allowing us to examine the sensitivity of model O<sub>3</sub>-CO correlations to input meteorological  
13 data. To understand how various emissions drive global O<sub>3</sub>-CO correlation patterns, we also  
14 investigated the sensitivity of GMI/MERRA model-calculated O<sub>3</sub> and CO concentrations and their  
15 correlations to emission types.

16 We evaluated GMI-simulated tropospheric O<sub>3</sub> vertical profiles and tropospheric O<sub>3</sub>  
17 columns (TOCs) with those from ozonesonde and satellite observations, respectively. To aid in  
18 the evaluation, model simulations of radionuclide tracers (<sup>222</sup>Rn, <sup>210</sup>Pb, and <sup>7</sup>Be) were used to  
19 illustrate the differences in convection, stratospheric influence, and large-scale subsidence among  
20 three meteorological data sets. Among the three GMI simulations, GMI/GEOS4-simulated O<sub>3</sub>  
21 concentrations are in best agreement with the observations. GMI/MERRA underestimates O<sub>3</sub> in  
22 the NH high-latitude UT due to weak STE, and overestimates O<sub>3</sub> in the SH subtropics due to



1 tropical deep convection being too shallow, which results in less low-O<sub>3</sub> air transported from LT  
2 to MT/UT, as well as excessive NO<sub>x</sub> emissions from lightning. The latitudinal distribution of  
3 model biases in TOCs relative to satellite observations is consistent with the results from model  
4 evaluations with ozonesonde O<sub>3</sub> profiles.

5 We evaluated GMI simulated O<sub>3</sub> and CO concentrations with TES observations at 618 hPa  
6 where TES has most sensitivity. TES observed O<sub>3</sub> enhancements over the NH mid-latitudes  
7 (including continental outflow regions), the Middle East, and the subtropical southern Africa and  
8 Atlantic. All simulations well capture the global spatial distribution of O<sub>3</sub> at 618 hPa, but appear  
9 to underestimate TES O<sub>3</sub> observations over southern Africa and its outflow region. GMI/fvGCM  
10 simulates the highest O<sub>3</sub> concentrations at NH mid-/high-latitudes, especially the Asian continent  
11 due to strong STE whereas it simulates the lowest O<sub>3</sub> concentrations in the southern tropics and  
12 subtropics due to weak STE and low lightning NO<sub>x</sub> emissions. GMI/MERRA simulates the highest  
13 O<sub>3</sub> concentrations in the southern subtropics, especially southern Africa due to high lightning NO<sub>x</sub>  
14 emissions and, to a lesser extent, strong convection. GMI/fvGCM underestimates the O<sub>3</sub> minimum  
15 in the tropical western Pacific and eastern Indian Ocean. Considering the positive bias in TES O<sub>3</sub>  
16 at NH mid-latitudes, GMI/fvGCM appears to overestimate O<sub>3</sub> over the East Asian outflow region  
17 due to too fast STE whereas GMI/GEOS4 and GMI/MERRA simulate O<sub>3</sub> enhancements  
18 reasonably well in East Asia and its downwind regions. All three simulations significantly  
19 underestimate TES-observed CO enhancements at NH mid-latitudes, but simulate better CO  
20 enhancements over the tropical biomass burning regions.

21 The three GMI simulations all show strong positive O<sub>3</sub>-CO correlations at 618 hPa over  
22 the NH mid-latitude continental outflow regions and the SH biomass burning outflow regions, as  
23 shown by TES observations. Generally, positive O<sub>3</sub>-CO correlations are simulated in downwind



1 of polluted regions due to photochemical production of  $O_3$  from its precursors. However, owing  
2 to significant influences from the stratosphere and subsidence from UT/LS over these regions,  
3 mixing of stratospheric air with polluted (anthropogenic or biomass burning) air masses is  
4 associated with strong positive  $O_3$ -CO correlations with large  $dO_3/dCO$  enhancement ratios.  
5 Strong positive  $O_3$ -CO correlations are also simulated over the Indonesian biomass burning region  
6 where deep convection occurs, but the  $dO_3/dCO$  enhancement ratios are smaller than those in the  
7 NH mid-latitude continental outflow regions. The latter reflects the lower efficiency of  $NO_x$   
8 emissions from biomass burning. Strong negative  $O_3$ -CO correlations over northern and central  
9 Africa, tropical Atlantic, and tropical eastern and western Pacific in all simulations result from  
10 convective transport of biomass burning air masses with low- $O_3$ , and consumption of  $O_3$  along  
11 with production of CO due to oxidation of biogenic hydrocarbons (e.g., isoprene under low  $NO_x$   
12 conditions). The simulated negative  $O_3$ -CO correlations over the Asian continent, including the  
13 Middle East, are partly attributed to stratospheric influence and/or subsidence from UT/LS. High-  
14  $O_3$  and low-CO associated with stratospherically influenced air lead to strong negative correlations  
15 with large  $dO_3/dCO$  ratios. On the other hand, over Southwest China, monsoonal convective lifting  
16 of air masses with high-CO and low- $O_3$  results in negative  $O_3$ -CO correlations. By contrast, TES  
17  $O_3$  and CO concentrations at 618 hPa either miss such negative correlations (i.e., tropical  
18 convective regions) or only show weak negative correlations over much narrower areas (i.e., the  
19 Tibetan Plateau and northern Africa).

20 TES-observed  $O_3$  and CO concentrations at 618 hPa show highest positive correlations  
21 with large regression slopes over the western Pacific, and relatively high correlations over North  
22 America, the Middle East, northern South America, central and southern Africa, and continental  
23 outflow regions. Negative correlations are observed in parts of the Asian continent (Tibetan



1 Plateau), northern Africa, and SH mid-latitudes. All model output sampled along the TES orbit  
2 track capture the observed positive O<sub>3</sub>-CO correlations over the NH mid-latitude continental  
3 outflow regions, southern Africa, western Indian Ocean, subtropical South Atlantic, northern  
4 South America, and tropical eastern Pacific . While all simulations show strong negative  
5 correlations over the Tibetan Plateau, northern Africa, northern subtropical eastern Pacific, and  
6 Caribbean, TES O<sub>3</sub> and CO concentrations at 618 hPa only show weak negative correlations over  
7 much narrower areas (i.e., the Tibetan Plateau and northern Africa).

8 We performed sensitivity simulations with GMI/MERRA to investigate the effect of  
9 individual emission types on model-calculated O<sub>3</sub>-CO correlations at 618 hPa. Results show that  
10 fossil fuel emissions increase global O<sub>3</sub> and CO concentrations and are responsible for the strong  
11 positive correlations over the NH continental outflow regions. Both biomass burning and biogenic  
12 emissions significantly increase global CO concentrations. Biomass burning emissions increase  
13 O<sub>3</sub> concentrations in the easterly outflow in the tropical South America and Central Africa, in the  
14 westerly outflow in the southern subtropics, and over Indonesia. Biogenic emissions increase O<sub>3</sub>  
15 concentrations in the NH subtropics and mid-latitudes, but decrease O<sub>3</sub> concentrations in tropical  
16 South America, tropical Africa, and Indonesia. The decreases mainly reflect the fact that O<sub>3</sub> is  
17 consumed during the atmospheric oxidation process of isoprene under low NO<sub>x</sub> conditions.  
18 Biomass burning emissions are responsible for the positive correlations in the SH mid- and high-  
19 latitudes and negative correlations over part of the tropical western Pacific, Bay of Bengal, NH  
20 subtropical Atlantic, and NH high latitudes. Biogenic emissions have relatively smaller impact on  
21 the correlations than other emissions do, but are largely responsible for the negative O<sub>3</sub>-CO  
22 correlations over the tropical eastern Pacific. Lightning NO<sub>x</sub> emissions lead to large increases in  
23 O<sub>3</sub> concentrations at NH subtropics and mid-latitudes, and at SH tropics and subtropics, especially



1 in the regions of subsidence. We find that lightning  $\text{NO}_x$  emissions weaken both positive  $\text{O}_3$ -CO  
2 correlations at mid- and high-latitudes and negative correlations in the tropics, and change weak  
3 positive correlations to negative in various areas. This result contrasts with that of previous studies.

4 This study demonstrates the utility of  $\text{O}_3$ -CO correlations to constrain the sources of  
5 tropospheric  $\text{O}_3$  in global 3-D models. Our model simulations driven by three input meteorological  
6 data sets show significantly different global and regional distributions of  $\text{O}_3$  and CO concentrations  
7 during boreal summer. For instance, GMI/fvGCM simulations show higher  $\text{O}_3$  concentrations in  
8 the NH and lower CO concentrations than other simulations. Despite such differences, all  
9 simulations show similar patterns of  $\text{O}_3$ -CO correlations on a global scale. The regional features  
10 of the correlations, however, are often different due to the discrepancies in various meteorological  
11 processes (e.g., convection, STE, subsidence). In particular, GMI/MERRA simulates broader areas  
12 of strong negative  $\text{O}_3$ -CO correlations at 618 hPa in the tropics than GMI/fvGCM and  
13 GMI/GEOS4 do due to stronger tropical convection in the LT/MT. In this sense,  $\text{O}_3$ -CO  
14 correlations can be used to constrain better the sources of regional tropospheric  $\text{O}_3$  in global models,  
15 especially for convective regions than  $\text{O}_3$  and CO observations individually. Future work will  
16 examine the driving factors for  $\text{O}_3$ -CO correlations in other seasons.

17

#### 18 **Data availability**

19 A description of the model output and observational data used in this paper can be found in Sect.  
20 2 and they are available upon request by contacting Hongyu Liu ([hongyu.liu-1@nasa.gov](mailto:hongyu.liu-1@nasa.gov)).

21



1 **Acknowledgements.** This work was supported by the NASA Modeling, Analysis, and Prediction  
2 (MAP) program and NASA Atmospheric Composition Modeling and Analysis Program  
3 (ACMAP). NASA Center for Computational Sciences (NCCS) provided supercomputing  
4 resources. TES data products are distributed by NASA Langley Atmospheric Science Data Center.

5

## 6 **References**

7

8 Allen, D., Pickering, K., Duncan, B., and Damon, M.: Impact of lightning NO emissions on North  
9 American photochemistry as determined using the Global Modeling Initiative (GMI) model,  
10 *J. Geophys. Res.*, *115*, D22301, doi:10.1029/2010JD014062, 2010.

11 Anderson, B. E., Gregory, G. L., Barrick, J. D. W., Collins, J. E. Jr., Sachse, G. W., Bagwell, D.,  
12 Shipham, M. C., Bradshaw, J. D., and Sandholm, S. T.: The impact of U.S. continental  
13 outflow on ozone and aerosol distributions over the western Atlantic, *J. Geophys. Res.*,  
14 *98*(D12), 23,477–23,489, doi:10.1029/93JD01208, 1993.

15 Beer, R., Glavich, T. A., and Rider, D. M.: Tropospheric emission spectrometer for the Earth  
16 Observing System's Aura Satellite, *Appl. Optics*, *40*, 2356–2367, 2001.

17 Beer, R.: TES on the Aura mission: Scientific objectives, measurements, and analysis overview,  
18 *IEEE T. Geosci. Remote*, *44*, 1102–1105, doi:10.1109/tgrs.2005.863716, 2006.

19 Bowman, K. W., Steck, T., Worden, H. M., Worden, J., Clough, S., and Rodgers, C.: Capturing  
20 time and vertical variability of tropospheric ozone: A study using TES nadir retrievals, *J.*  
21 *Geophys. Res.*, *107*(D23), 4723, doi:10.1029/2002JD002150, 2002.

22 Bowman, K. W., et al.: Tropospheric emission spectrometer: Retrieval method and error analysis,  
23 *IEEE T. Geosci. Remote*, *44*, 1297–1307, doi:10.1109/tgrs.2006871234, 2006.



- 1 Benkovitz, C. M., Scholtz, M. T., Pacyna, J., Tarrasón, L., Dignon, J., Voldner, E. C., Spiro, P.  
2 A., Logan, J. A., and Graedel, T. E.: Global gridded inventories of anthropogenic emissions  
3 of sulfur and nitrogen, *J. Geophys. Res.*, *101*(D22), 29239–29253, doi:10.1029/96JD00126,  
4 1996.
- 5 Bey, I., Jacob, D.J., Yantosca, R.M., Logan, J.A., Field, B., Fiore, A.M., Li, Q., Liu, H., Mickley,  
6 L.J., and Schultz, M.: Global modeling of tropospheric chemistry with assimilated  
7 meteorology: Model description and evaluation, *J. Geophys. Res.*, *106*, 23,073–23,096, 2001.
- 8 Bloom, S., Silva, A. da, Dee, D., Bosilovich, M., Chern, J.-D., Pawson, S., Schubert, S.,  
9 Sienkiewicz, M., Stajner, I., Tan, W.-W., and Wu, M.-L.: Documentation and Validation of  
10 the Goddard Earth Observing System (GEOS) Data Assimilation System - Version 4.  
11 *Technical Report Series on Global Modeling and Data Assimilation* (Editor Max J. Suarez),  
12 NASA/TM-2005-104606, Vol. 26, NASA Goddard Space Flight Center, Greenbelt,  
13 Maryland, April 2005, 2005.
- 14 Chin, M., Jacob, D. J., Munger, J. W., Parrish, D. D., and Doddridge, B. G.: Relationship of ozone  
15 and carbon monoxide over North America, *J. Geophys. Res.*, *99*(D7), 14,565–14,573,  
16 doi:10.1029/94JD00907, 1994.
- 17 Chandra, S., Ziemke, J. R., Duncan, B. N., Diehl, T. L., Livesey, N. J., and Froidevaux, L.: Effects  
18 of the 2006 El Niño on tropospheric ozone and carbon monoxide: implications for dynamics  
19 and biomass burning, *Atmos. Chem. Phys.*, *9*, 4239–4249, doi:10.5194/acp-9-4239-2009,  
20 2009.
- 21 Collins Jr., J. E., Anderson, B. E., Sachse, G. W., J. Barrick, D. W., Wade, L. O., Burney, L. G.,  
22 and Hill, G. F.: Atmospheric fine structure during GTE TRACE A: Relationships among



- 1 ozone, carbon monoxide, and water vapor, *J. Geophys. Res.*, *101*(D19), 24307–24316,  
2 doi:10.1029/96JD02180, 1996.
- 3 Considine, D. B., Bergmann, D. J., and Liu, H.: Sensitivity of Global Modeling Initiative  
4 chemistry and transport model simulations of radon-222 and lead-210 to input  
5 meteorological data, *Atmos. Chem. Phys.*, *5*, 3389-3406, doi:10.5194/acp-5-3389-2005,  
6 2005.
- 7 Considine, D. B., Logan, J. A., and Olsen, M. A.: Evaluation of near-tropopause ozone  
8 distributions in the Global Modeling Initiative combined stratosphere/troposphere model  
9 with ozonesonde data, *Atmos. Chem. Phys.*, *8*, 2365-2385, doi:10.5194/acp-8-2365-2008,  
10 2008.
- 11 Cooper, O. R., Moody, J. L., Parrish, D. D., Trainer, M., Holloway, J. S., Hübler, G., Fehsenfeld,  
12 F. C., and Stohl, A.: Trace gas composition of midlatitude cyclones over the western North  
13 Atlantic Ocean: A seasonal comparison of O<sub>3</sub> and CO, *J. Geophys. Res.*, *107*(D7),  
14 doi:10.1029/2001JD000902, 2002.
- 15 Dibb, J. E., Meeker, L. D., Finkel, R. C., Southon, J. R., Caffee, M. W., and Barrie, L. A.:  
16 Estimation of stratospheric input to the Arctic troposphere: <sup>7</sup>Be and <sup>10</sup>Be in aerosols at Alert,  
17 Canada, *J. Geophys. Res.*, *99*, 12,855-12,864, 1994.
- 18 Douglass, A.R., Prather, M.J., Hall, T.M., Strahan, S.E., Rasch, P.J., Sparling, L.C., Coy, L., and  
19 Rodriguez, J.M.: Choosing meteorological input for the global modeling initiative  
20 assessment of high-speed aircraft, *J. Geophys. Res.*, *104*(D22), 27,545-27,564, 1999.
- 21 Douglass, A. R., Stolarski, R. S., Strahan, S. E., and Connell, P. S.: Radicals and reservoirs in the  
22 GMI chemistry and transport model: Comparison to measurements, *J. Geophys. Res.*, *109*,  
23 D16302, doi:10.1029/2004JD004632, 2004.



- 1 Duncan, B. N., Martin, R., Staudt, A., Yevich, R., and Logan, J.: Interannual and Seasonal  
2 Variability of Biomass Burning Emissions Constrained by Satellite Observations, *J.*  
3 *Geophys. Res.*, *108*(D2), 4100, doi:10.1029/2002JD002378, 2003.
- 4 Duncan, B. N., Strahan, S. E., Yoshida, Y., Steenrod, S. D., and Livesey, N.: Model study of the  
5 cross-tropopause transport of biomass burning pollution, *Atmos. Chem. Phys.*, *7*, 3713-3736,  
6 doi:10.5194/acp-7-3713-2007, 2007a.
- 7 Duncan, B. N., Logan, J. A., Bey, I., Megretskaia, I. A., Yantosca, R. M., Novelli, P. C., Jones, N.  
8 B., and Rinsland, C. P.: Global budget of CO, 1988–1997: Source estimates and validation  
9 with a global model, *J. Geophys. Res.*, *112*, D22301, doi:10.1029/2007JD008459, 2007b.
- 10 Duncan, B. N., West, J. J., Yoshida, Y., Fiore, A. M., and Ziemke, J. R.: The influence of  
11 European pollution on ozone in the Near East and northern Africa, *Atmos. Chem. Phys.*, *8*,  
12 2267-2283, doi:10.5194/acp-8-2267-2008, 2008.
- 13 Fan, J. and Zhang, R.: Atmospheric oxidation mechanism of Isoprene, *Environ. Chem.*, *1*, 140-  
14 149, doi: 10.1071/EV04045, 2004.
- 15 Fehsenfeld, F. C., Daum, P., Leaitch, W. R., Trainer, M., Parrish, D. D., and Hübler, G.: Transport  
16 and processing of O<sub>3</sub> and O<sub>3</sub> precursors over the North Atlantic: An overview of the 1993  
17 North Atlantic Regional Experiment (NARE) summer intensive, *J. Geophys. Res.*, *101*(D22),  
18 28,877–28,891, doi:10.1029/96JD01113, 1996.
- 19 Fishman, J., and Seiler, W.: Correlative nature of ozone and carbon monoxide in the troposphere:  
20 Implications for the tropospheric ozone budget, *J. Geophys. Res.*, *88*, 3662–3670, 1983.
- 21 Fishman, J., Wozniak, A. E., and Creilson, J. K.: Global distribution of tropospheric ozone from  
22 satellite measurements using the empirically corrected tropospheric ozone residual



- 1            technique: Identification of the regional aspects of air pollution, *Atmos. Chem. Phys.*, **3**, 893-  
2            907, 2003.
- 3    Guenther, A., Karl, T., Harley, P., Wiedinmyer, C., Palmer, P.I., and Geron, C.: Estimates of global  
4            terrestrial isoprene emissions using MEGAN (Model of Emissions of Gases and Aerosols  
5            from Nature), *Atmos. Chem. Phys.*, **6**, 3181-3210, 2006.
- 6    Hack, J. J.: Parameterization of moist convection in the National Center for Atmospheric Research  
7            Community Climate Model (CCM2), *J. Geophys. Res.*, **99**, 5551–5568, 1994.
- 8    Honrath, R. E., Owen, R. C., Val Martín, M., Reid, J. S., Lapina, K., Fialho, P., Dziobak, M. P.,  
9            Kleissl, J., and Westphal, D. L.: Regional and hemispheric impacts of anthropogenic and  
10           biomass burning emissions on summertime CO and O<sub>3</sub> in the North Atlantic lower free  
11           troposphere, *J. Geophys. Res.*, **109**, D24310, doi:10.1029/2004JD005147, 2004.
- 12   Hsu, J., Prather, M. J., Wild, O., Sundet, J. K., Isaksen, I. S. A., Browell, E. V., Avery, M. A., and  
13           Sachse, G. W.: Are the TRACE-P measurements representative of the western Pacific during  
14           March 2001?, *J. Geophys. Res.*, **109**(D2), D02314, doi:10.1029/2003JD004002, 2004.
- 15   Jacob D. J., and Wofsy, S. C.: Budgets of Reactive Nitrogen, Hydrocarbons, and Ozone Over the  
16           Amazon Forest During the Wet Season, *J. Geophys. Res.*, **95**, 16,737-16,754, 1990.
- 17   Jacob, D. J., et al.: Evaluation and inter-comparison of global atmospheric transport models using  
18           2•Rn and other short-lived tracers, *J. Geophys. Res.*, **102**, 5953-5970, 1997.
- 19   Jaffe, D. A., Honrath, R. E., Zhang, L., Akimoto, H., Shimizu, A., Mukai, H., Murano, K.,  
20           Hatakeyama, S., and Merrill, J.: Measurements of NO, NO<sub>y</sub>, CO and O<sub>3</sub> and estimation of  
21           the ozone production rate at Oki Island, Japan, during PEM-West, *J. Geophys. Res.*, **101**(D1),  
22           2037–2048, doi:10.1029/95JD01699, 1996.



- 1 Kim, P. S., Jacob, D. J., Liu, X., Warner, J. X., Yang, K., Chance, K., Thouret, V., and  
2 Nedelec, P.: Global ozone–CO correlations from OMI and AIRS: constraints on tropospheric  
3 ozone sources, *Atmos. Chem. Phys.*, *13*, 9321–9335, doi:10.5194/acp-13-9321-2013, 2013.
- 4 Kinnison, D. E., et al.: The Global Modeling Initiative assessment model: Application to high-  
5 speed civil transport perturbation, *J. Geophys. Res.*, *106*(D2), 1693–1711,  
6 doi:10.1029/2000JD900406, 2001.
- 7 Koch, D. M., and Mann, M. E.: Spatial and temporal variability of  $^7\text{Be}$  surface concentration,  
8 *Tellus, Ser. B*, *48*, 387–396, 1996.
- 9 Li, Q., Jacob, D. J., Bey, I., Palmer, P. I., Duncan, B. N., Field, B. D., Martin, R. V., Fiore, A.  
10 M., Yantosca, R. M., Parrish, D. D., Simmonds, P. G., and Oltmans, S. J.: Transatlantic  
11 transport of pollution and its effects on surface ozone in Europe and North America, *J.*  
12 *Geophys. Res.*, *107*(D13), doi:10.1029/2001JD001422, 2002.
- 13 Lin, S.-J., and Rood, R. B.: Multidimensional flux-form semi-Lagrangian transport schemes, *Mon.*  
14 *Weather Rev.*, *124*, 2046–2070, 1996.
- 15 Liu, H., Jacob, D. J., Bey, I., and Yantosca, R. M.: Constraints from  $^{210}\text{Pb}$  and  $^7\text{Be}$  on wet  
16 deposition and transport in a global three-dimensional chemical tracer model driven by  
17 assimilated meteorological fields, *J. Geophys. Res.*, *106*(D11), 12109–12128,  
18 doi:10.1029/2000JD900839, 2001.
- 19 Liu, H., Considine, D. B., Horowitz, L. W., Crawford, J. H., Rodriguez, J. M., Strahan, S. E.,  
20 Damon, M. R., Steenrod, S. D., Xu, X., Kouatchou, J., Carouge, C., and Yantosca, R. M.:  
21 Using beryllium-7 to assess cross-tropopause transport in global models, *Atmos. Chem.*  
22 *Phys.*, *16*, 4641–4659, doi:10.5194/acp-16-4641-2016, 2016.



- 1 Liu, J., Logan, J. A., Jones, D. B. A., Livesey, N. J., Megretskaia, I., Carouge, C., and Nedelec, P.:  
2 Analysis of CO in the tropical troposphere using Aura satellite data and the GEOS-Chem  
3 model: insights into transport characteristics of the GEOS meteorological products, *Atmos.*  
4 *Chem. Phys.*, *10*, 12207-12232, doi:10.5194/acp-10-12207-2010, 2010.
- 5 Logan, J. A. (1999), An analysis of ozonesonde data for the troposphere: Recommendations for  
6 testing 3-D models and development of a gridded climatology for tropospheric ozone, *J.*  
7 *Geophys. Res.*, *104*, 16 115–16 149.
- 8 Lopez, J. P., Luo, M., Christensen, L. E., Loewenstein, M., Jost, H., Webster, C. R., and Osterman,  
9 G.: TES carbon monoxide validation during two AVE campaigns using the Argus and  
10 ALIAS instruments on NASA's WB-57F, *J. Geophys. Res.*, *113*, D16S47,  
11 doi:10.1029/2007JD008811, 2008.
- 12 Luo, M., et al.: TES carbon monoxide validation with DACOM aircraft measurements during  
13 INTEx-B 2006, *J. Geophys. Res.*, *112*, D24S48, doi:10.1029/2007JD008803, 2007a.
- 14 Luo, M., et al.: Comparison of carbon monoxide measurements by TES and MOPITT: Influence  
15 of a priori data and instrument characteristics on nadir atmospheric species retrievals, *J.*  
16 *Geophys. Res.*, *112*, D09303, doi:10.1029/2006JD007663, 2007b.
- 17 Mari, C., Jacob, D. J., and Bechtold, P.: Transport and scavenging of soluble gases in a deep  
18 convective cloud, *J. Geophys. Res.*, *105*, 22,255-22,267, 2000.
- 19 Mauzerall, D. L., Narita, D., Akimoto, H., Horowitz, L., Walters, S., Hauglustaine, D. A., and  
20 Brasseur, G.: Seasonal characteristics of tropospheric ozone production and mixing ratios  
21 over East Asia: A global three-dimensional chemical transport model analysis, *J. Geophys.*  
22 *Res.*, *105*(D14), 17,895–17,910, doi:10.1029/2000JD900087, 2000.



- 1 Moorthi S. and Suarez, M. J.: Relaxed Arakawa-Shubert. A Parameterization of moist convection  
2 for general circulation models, *Mon. Weather Rev.*, *120*, 978-1002, 1992.
- 3 Naja, M., Lal, S., and Chand, D.: Diurnal and seasonal variabilities in surface ozone at a high  
4 altitude site Mt Abu (24.6 degrees N, 72.7 degrees E, 1680 m asl) in India, *Atmos. Environ.*,  
5 *37*, 4205–4215, doi:10.1016/S1352-2310(03)00565-X, 2003.
- 6 Nassar, R., et al.: Validation of Tropospheric Emission Spectrometer (TES) nadir ozone profiles  
7 using ozonesonde measurements, *J. Geophys. Res.*, *113*, D15S17,  
8 doi:10.1029/2007JD008819, 2008.
- 9 Mao, H., and Talbot, R.: O<sub>3</sub> and CO in New England: Temporal variations and relationships, *J.*  
10 *Geophys. Res.*, *109*, D21304, doi:10.1029/2004JD004913, 2004,.
- 11 Osterman, G. B., Kulawik, S. S., Worden, H., Richards, N. A., Fisher, B. M., Eldering, A.,  
12 Shephard, M. W., Froidevaux, L., Labow, G., Luo, M., Herman, R. L., Bowman, K. W., and  
13 Thompson, A. M.: Validation of Tropospheric Emission Spectrometer (TES) measurements  
14 of the total, stratospheric, and tropospheric column abundance of ozone, *J. Geophys. Res.*,  
15 *113*, D15S16, doi:10.1029/2007JD008801, 2008.
- 16 Parrington, M., Jones, D. B. A., Bowman, K. W., Horowitz, L. W., Thompson, A. M., Tarasick,  
17 D. W., and Witte, J. C.: Estimating the summertime tropospheric ozone distribution over  
18 North America through assimilation of observations from the Tropospheric Emission  
19 Spectrometer, *J. Geophys. Res.*, *113*, D18307, doi:10.1029/2007JD009341, 2008.
- 20 Parrish, D. D., Holloway, J. S., Trainer, M., Murphy, P. C., Forbes, G. L., and Fehsenfeld, F. C.:  
21 Export of North American Ozone Pollution to the North Atlantic Ocean, *Science*, *259*, 1436–  
22 1439, 1993.



- 1 Parrish, D. D., Trainer, M., Holloway, J. S., Yee, J. E., Warshawsky, M. S., and Fehsenfeld, F.  
2 C.: Relationships between ozone and carbon monoxide at surface sites in the North Atlantic  
3 region, *J. Geophys. Res.*, *103*(D11), 13357–13376, 1998.
- 4 Real, E., Law, K. S., Schlager, H., Roiger, A., Huntrieser, H., Methven, J., Cain, M., Holloway, J.,  
5 Neuman, J. A., Ryerson, T., Flocke, F., Gouw, J. de, Atlas, E., Donnelly, S., and Parrish, D.:  
6 Lagrangian analysis of low altitude anthropogenic plume processing across the North  
7 Atlantic, *Atmos. Chem. Phys.*, *8*, 7737– 7754, doi:10.5194/acp-8-7737-2008, 2008.
- 8 Rotman, D. A., et al.: Global Modeling Initiative assessment model: Model description, integration,  
9 and testing of the transport shell, *J. Geophys. Res.*, *106*, 1669–1691, 2001.
- 10 Schoeberl, M. R., Duncan, B. N., Douglass, A. R., Waters, J., Livesey, N., Read, W., and Filipiak,  
11 M.: The carbon monoxide tape recorder, *Geophys. Res. Lett.*, *33*, L12811,  
12 doi:10.1029/2006GL026178, 2006.
- 13 Seinfeld, J. H., and Pandis, S. N.: Atmospheric Chemistry and Physics, Wiley, New York, 1998.
- 14 Shim, C., Li, Q., Luo, M., Kulawik, S., Worden, H., Worden, J., Eldering, A., Diskin, G., Sachse,  
15 G., Weinheimer, A., Knapp, D., Montzca, D., and Campos, T.: Satellite observations of  
16 Mexico City pollution outflow from the Tropospheric Emissions Spectrometer (TES),  
17 *Atmos. Environ.*, *43*, 1540–1547, doi:10.1016/j.atmosenv.2008.11.026, 2009.
- 18 Shindell, D. T., et al.: Multimodel simulations of carbon monoxide: Comparison with observations  
19 and projected near-future changes, *J. Geophys. Res.*, *111*, D19306,  
20 doi:10.1029/2006JD007100, 2006.
- 21 Strahan, S. E., Duncan, B. N., and Hoor, P.: Observationally derived transport diagnostics for the  
22 lowermost stratosphere and their application to the GMI chemistry and transport model,  
23 *Atmos. Chem. Phys.*, *7*, 2435–2445, doi:10.5194/acp-7-2435-2007, 2007.



- 1 Thompson, A. M., Pickering, K. E., McNamara, D. P., Schoeberl, M. R., Hudson, R. D., Kim, J.  
2 H., Browell, E. V., Kirchhoff, V. W. J. H., and Nganga, D.: Where did tropospheric ozone  
3 over southern Africa and the tropical Atlantic come from in October 1992? Insights from  
4 TOMS, GTE TRACE A, and SAFARI 1992, *J. Geophys. Res.*, *101*(D19), 24,251–24,278,  
5 doi:10.1029/96JD01463, 1996.
- 6 Thompson, A. M., Witte, J. C., McPeters, R. D., et al.: Southern Hemisphere Additional  
7 Ozonesondes (SHADOZ) 1998–2000 tropical ozone climatology – 1. Comparison with  
8 Total Ozone Mapping Spectrometer (TOMS) and ground-based measurements, *J. Geophys.*  
9 *Res.*, *108*(D2), 8238, doi:10.1029/2001JD000967, 2003.
- 10 Tsutsumi, Y., and Matsueda, H.: Relationship of ozone and CO at the summit of Mt. Fuji (35.35  
11 degrees N, 138.73 degrees E, 3776 m above sea level) in summer 1997, *Atmos. Environ.*, *34*,  
12 553– 561, 2000.
- 13 Voulgarakis, A., Telford, P. J., Aghedo, A. M., Braesicke, P., Faluvegi, G., Abraham, N. L.,  
14 Bowman, K. W., Pyle, J. A., and Shindell, D. T.: Global multi-year O<sub>3</sub>-CO correlation  
15 patterns from models and TES satellite observations, *Atmos. Chem. Phys.*, *11*, 5819-5838,  
16 doi:10.5194/acp-11-5819-2011, 2011.
- 17 Wang, T., Wong, H. L. A., Tang, J., Ding, A., Wu, W. S., and Zhang, X. C.: On the origin of  
18 surface ozone and reactive nitrogen observed at a remote mountain site in the northeastern  
19 Qinghai-Tibetan Plateau, western China, *J. Geophys. Res.*, *111*, D08303,  
20 doi:10.1029/2005JD006527, 2006.
- 21 Worden, J., Kulawik, S. S., Shephard, M. W., Clough, S. A., Worden, H., Bowman, K., and  
22 Goldman, A.: Predicted errors of tropospheric emission spectrometer nadir retrievals from



- 1 spectral window selection, *J. Geophys. Res.*, *109*, D09308, doi:10.1029/2004JD004522,  
2 2004.
- 3 Worden, H. M., et al.: Comparisons of Tropospheric Emission Spectrometer (TES) ozone profiles  
4 to ozonesondes: Methods and initial results, *J. Geophys. Res.*, *112*, D03309,  
5 doi:10.1029/2006JD007258, 2007.
- 6 Yevich, R., and Logan, J. A.: An assesment of biofuel use and burning of agricultural waste in the  
7 developing world, *Global Biogeochem. Cycles*, *17*, (4), 1095, doi:10.1029/2002GB001952,  
8 2003.
- 9 Zhang, G. J., and McFarlane, N. A.: Sensitivity of climate simulations to the parameterization of  
10 cumulus convection in the Canadian Climate Centre general circulation model, *Atmos.*  
11 *Ocean.*, *33*, 407–446, 1995.
- 12 Zhang, L., Jacob, D. J., Bowman, K. W., Logan, J. A., Turquety, S., Hudman, R. C., Li, Q., Beer,  
13 R., Worden, H. M., Rinsland, C. P., Kulawik, S. S., Lampel, M. C., Shephard, M. W., Fisher,  
14 B. M., Eldering, A., and Avery, M. A.: Ozone-CO correlations determined by the TES  
15 satellite instrument in continental outflow regions, *Geophys. Res. Lett.*, *33*, L18804,  
16 doi:10.1029/2006GL026399, 2006.
- 17 Zhang, L., Li, Q. B., Jin, J., Liu, H., Livesey, N., Jiang, J. H., Mao, Y., Chen, D., Luo, M. , and  
18 Chen, Y.: Impacts of 2006 Indonesian fires and dynamics on tropical upper tropospheric  
19 carbon monoxide and ozone, *Atmos. Chem. Phys.*, *11*, 10929-10946, doi:10.5194/acp-11-  
20 10929-2011, 2011 .
- 21 Zhang, L., Li, Q. B., Murray, L. T., Luo, M., Liu, H., Jiang, J. H., Mao, Y., Chen, D., Gao, M., and  
22 Livesey, N.: A tropospheric ozone maximum over the equatorial Southern Indian Ocean,  
23 *Atmos. Chem. Phys.*, *12*, 4279-4296, doi:10.5194/acp-12-4279-2012, 2012.



1 Ziemke, J.R., Chandra, S., Duncan, B. N., Froidevaux, L., Bhartia, P. K., Levelt, P. F., and Waters,  
2 J. W.: Tropospheric ozone determined from Aura OMI and MLS: Evaluation of  
3 measurements and comparison with the Global Modeling Initiative's Chemical Transport  
4 Model, *J. Geophys. Res.*, *111*, D19303, doi:10.1029/2006JD007089, 2006.

5

6

7

8

9

10

11

12

13

14

15

16

17

18

19

20

21

22

23

24

25

26

27



1

2

3

4

5

6

7 **Table 1.** Global lightning NO<sub>x</sub> emissions (Tg N/mon) during May – August in GMI CTM driven  
8 by three meteorological data sets (fvGCM, GEOS4, and MERRA)

	May	June	July	August
fvGCM	0.57 (0.03 <sup>a</sup> )	0.65 (0.02)	0.80 (0.03)	0.78 (0.05)
GEOS4	0.64 (0.05)	0.73 (0.07)	0.82 (0.03)	0.72 (0.05)
MERRA	0.49 (0.07)	0.69 (0.07)	0.81 (0.03)	0.78(0.04)

9

10 <sup>a</sup> Values in parenthesis denote lightning NO<sub>x</sub> emissions between 10°S and 70°S.

11

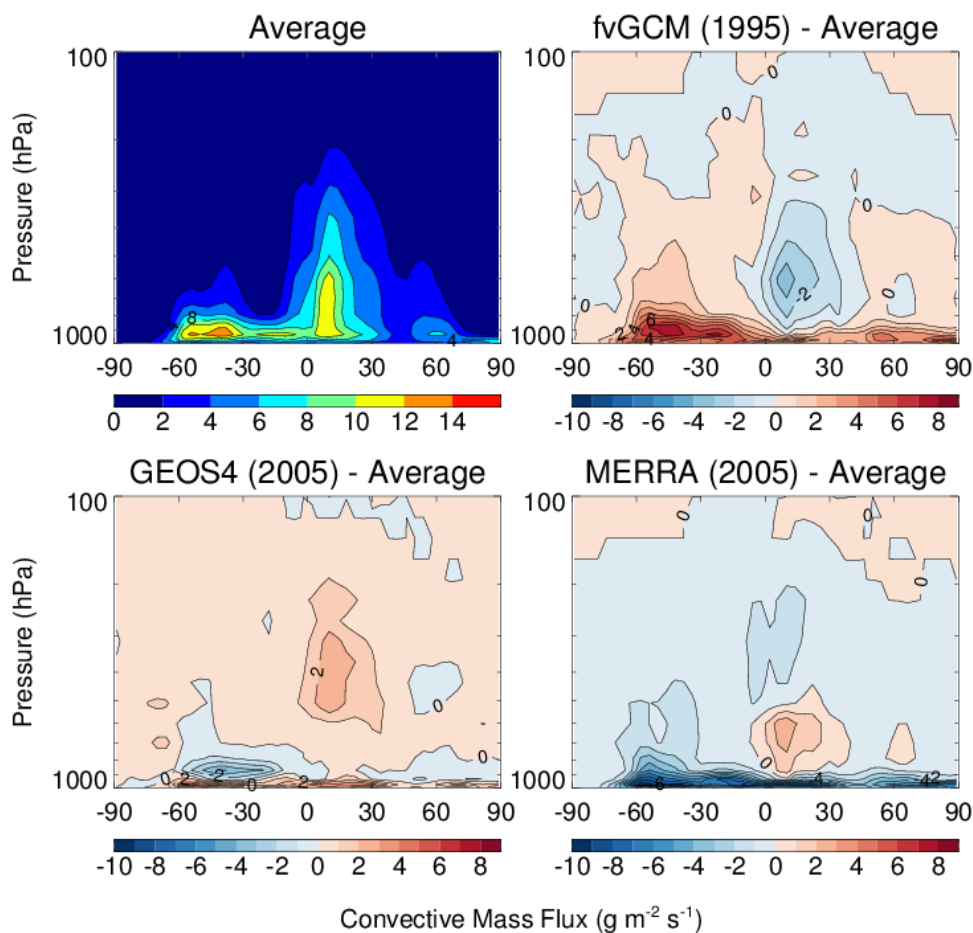
12

13

14



1  
2  
3

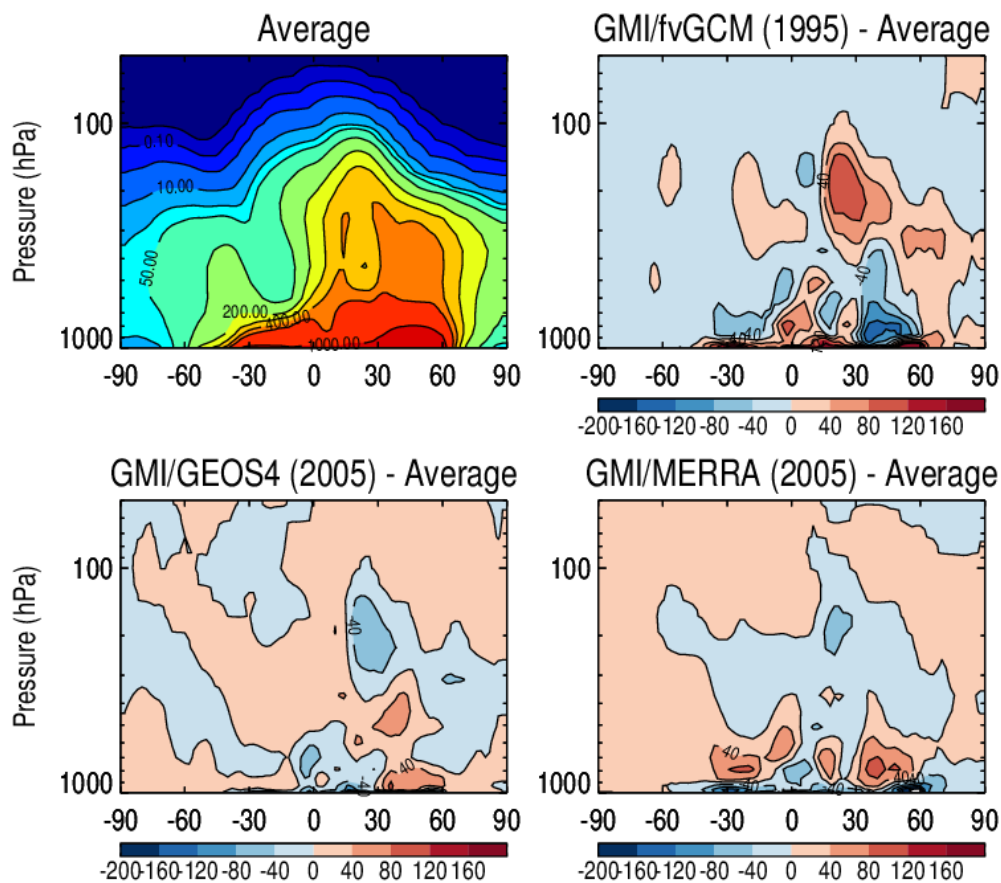


4  
5  
6  
7  
8  
9  
10  
11  
12

**Figure 1.** Latitude-height cross sections of zonal mean convective mass fluxes during July-August. The plot shows the values averaged over the fvGCM (1995), GEOS4 (2005), and MERRA (2005) meteorological data sets, as well as differences from the average.



1  
2

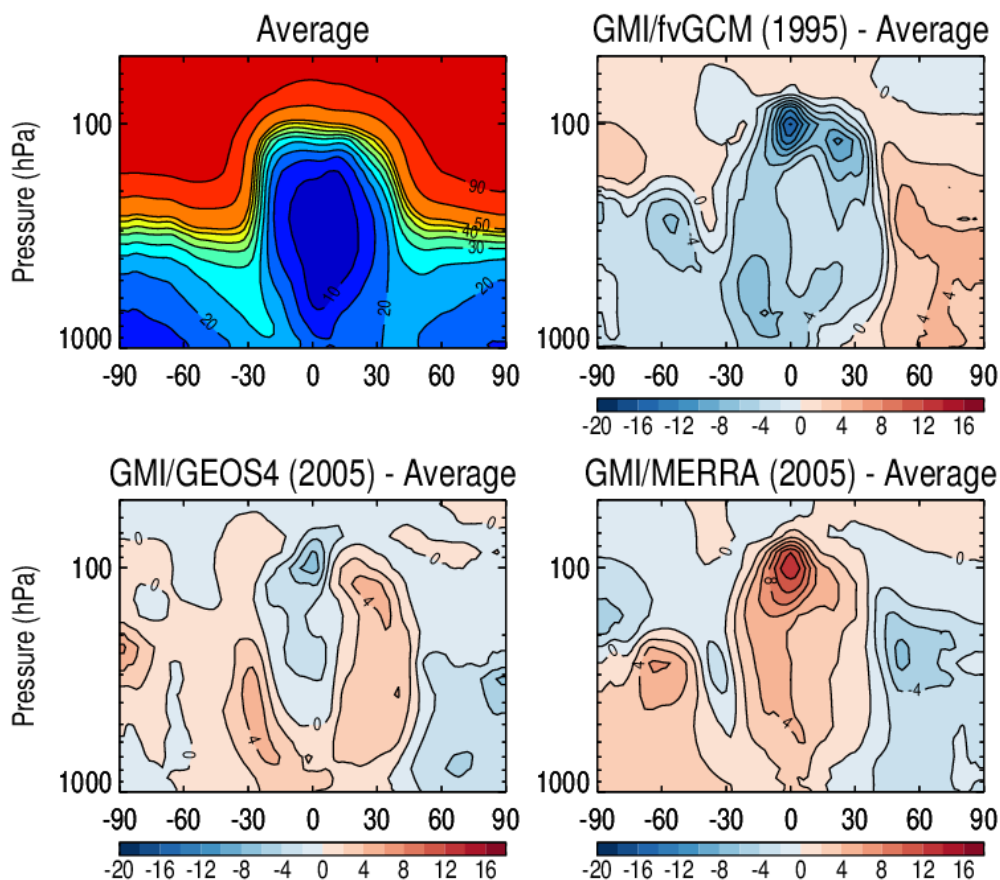


3  
4  
5  
6  
7  
8  
9  
10  
11  
12  
13  
14

**Figure 2.** Latitude-height cross sections of zonal mean  $^{222}\text{Rn}$  concentrations ( $\text{mBq SCM}^{-1}$ ) as simulated by GMI for July-August. The plot shows the values averaged over three simulations driven by the fvGCM (1995), GEOS4 (2005), and MERRA (2005) meteorological data sets, as well as differences of each simulation from the average.



1  
2  
3



4  
5

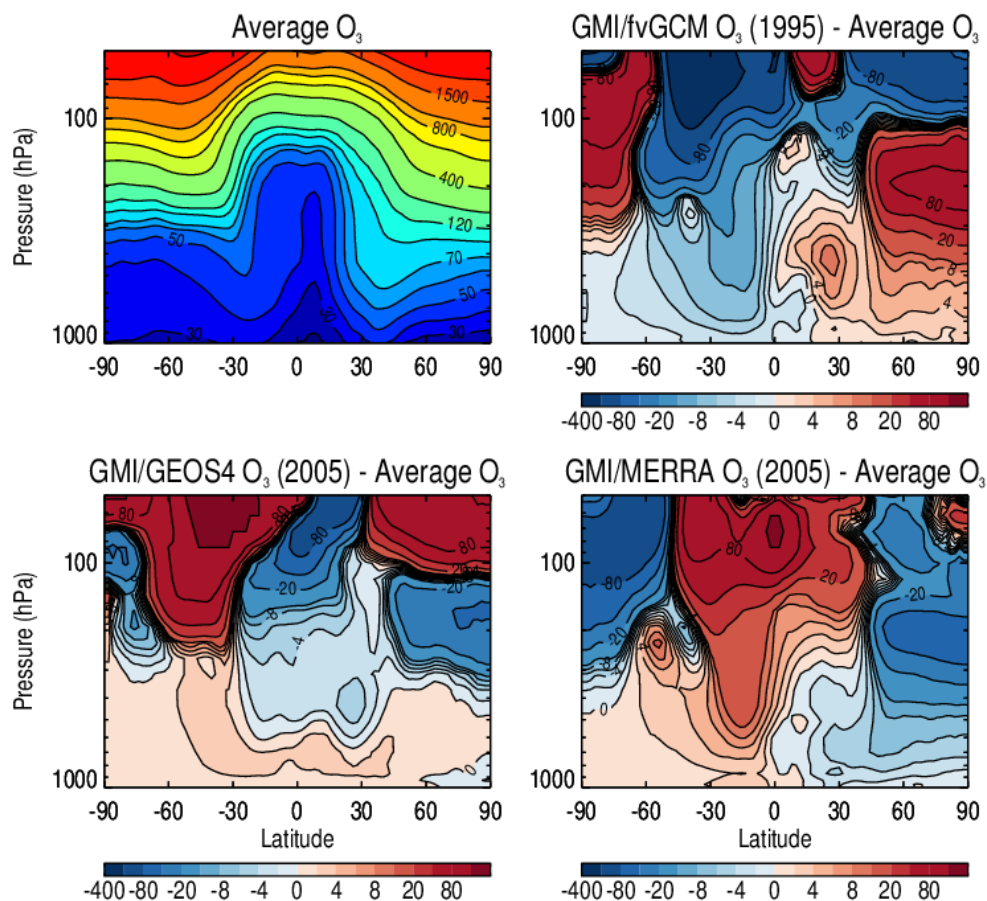
6 **Figure 3.** Same as **Figure 2**, but for stratospheric fraction (%) of zonal mean tropospheric  $^7\text{Be}$   
7 concentrations.

8  
9  
10  
11  
12  
13



1

2



3

4

5

**Figure 4.** Same as **Figure 2**, but for zonal mean ozone mixing ratios (ppbv).

6

7

8

9

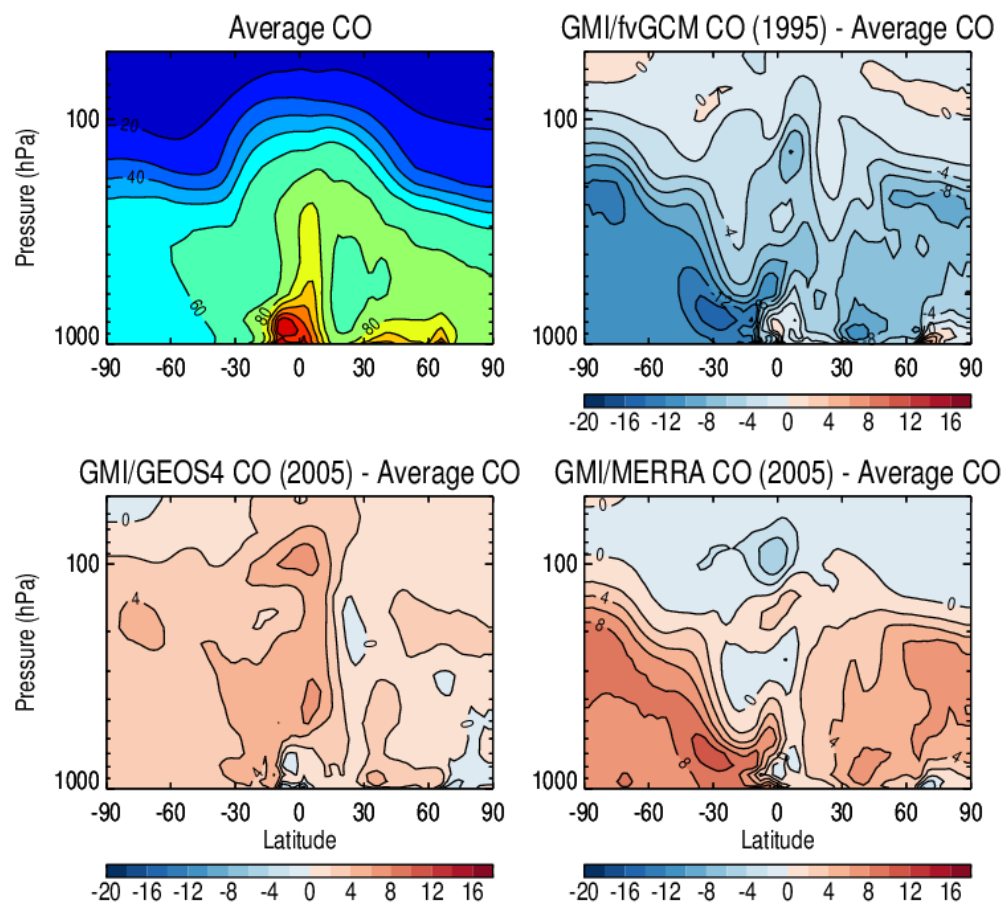
10

11



1

2



3

4

5

**Figure 5.** Same as **Figure 2**, but for zonal mean CO mixing ratios (ppbv).

6

7

8

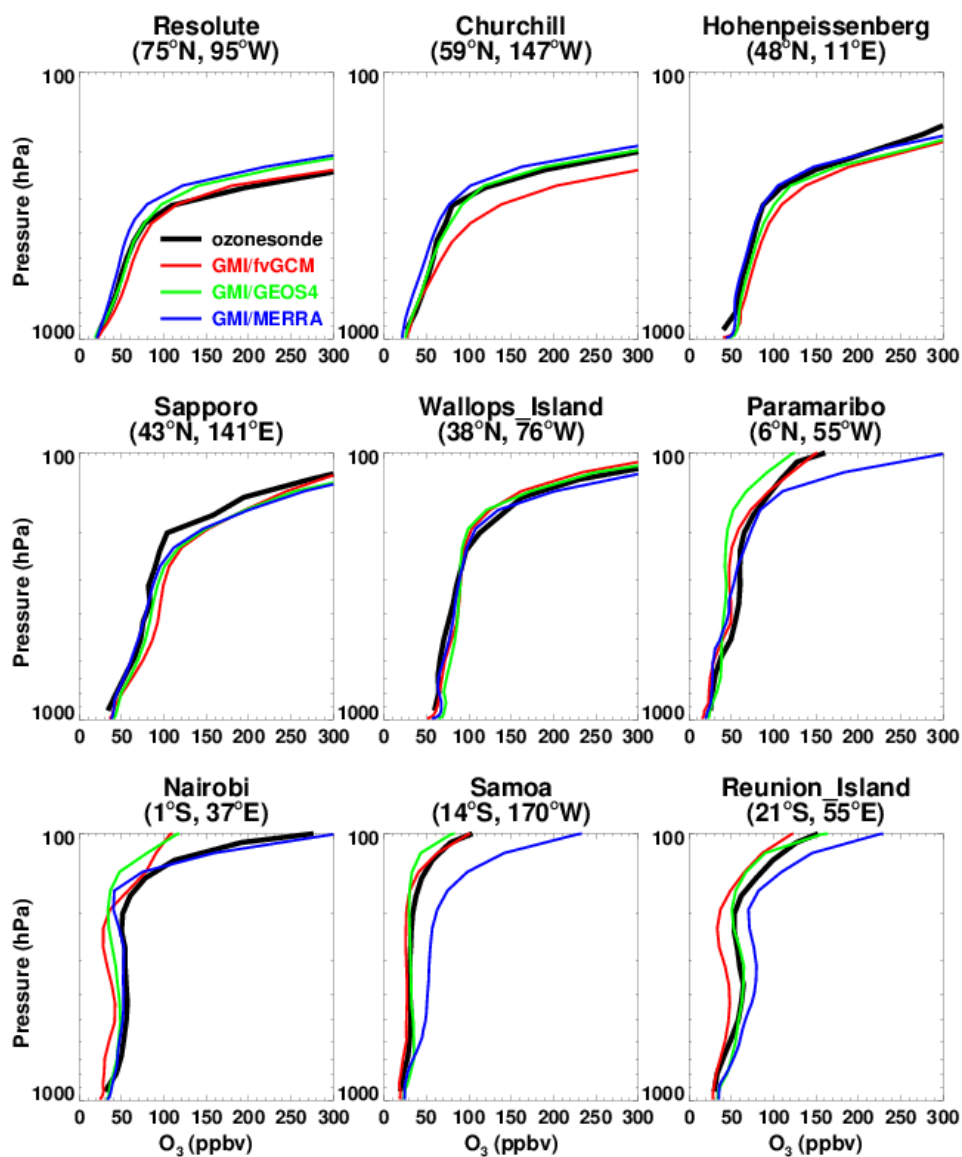
9

10

11



1



2

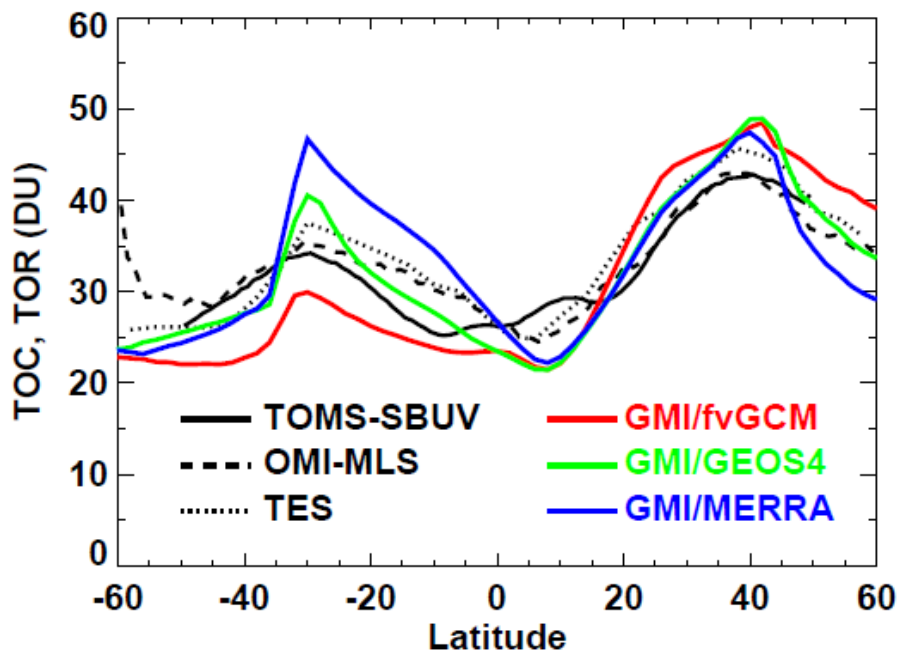
3

4 **Figure 6.** Comparisons of GMI simulated tropospheric ozone profiles (color lines) with  
5 ozonesonde observations (black line) for a range of latitudes. The model is driven by the fvGCM,  
6 GEOS4, and MERRA meteorological fields. Values are July–August average.

7



1

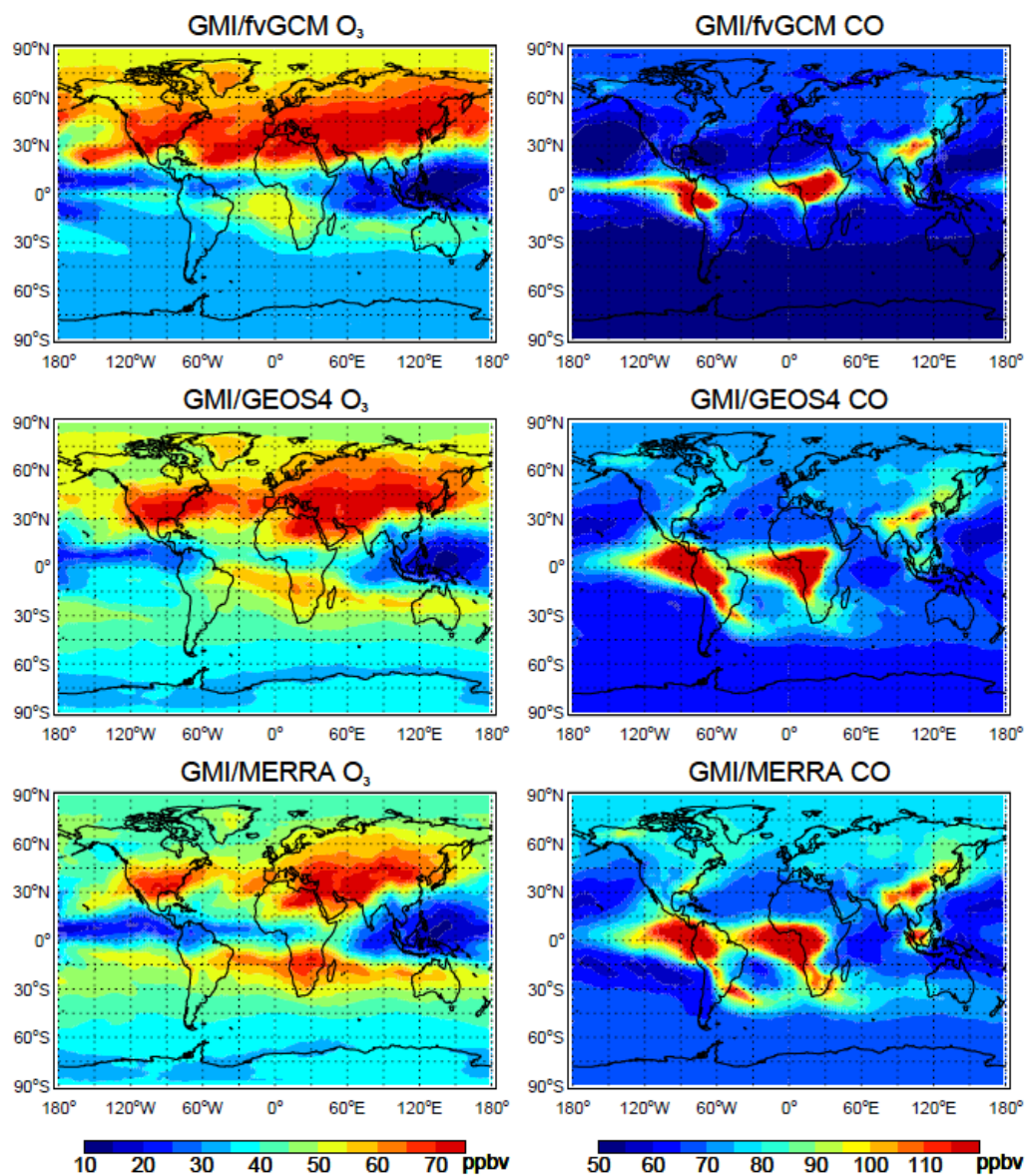


2

3

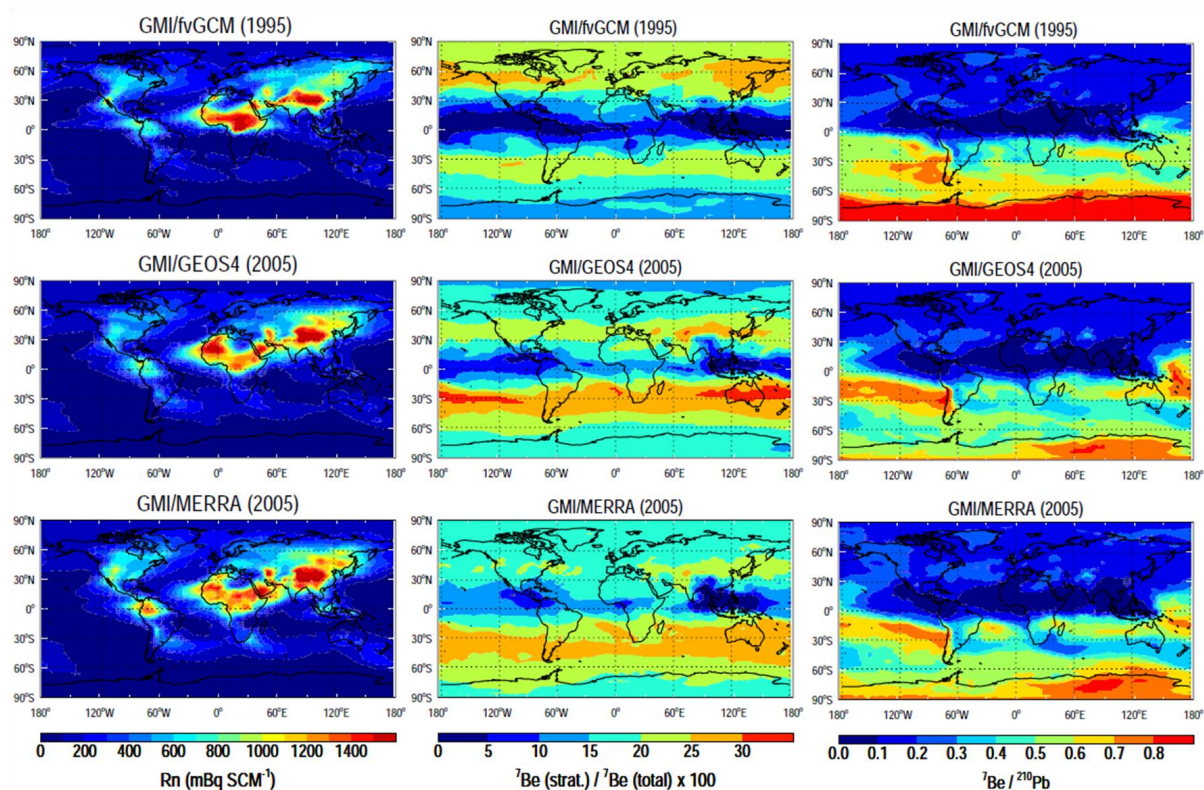
4 **Figure 7.** GMI simulated zonal mean tropospheric ozone columns (TOCs) compared with  
5 tropospheric ozone residuals (TORs) determined from TOMS/SBUV (July–August 1979–2005  
6 multi-year average) (Fishman et al., 2003), OMI/MLS (July–August 2005 average ) (Ziemke et al.,  
7 2006), and TOCs determined from TES retrievals (July–August 2005 average).

8



1  
2  
3

4 **Figure 8.** July-August mean mixing ratios of O<sub>3</sub> and CO (ppbv) at 618 hPa as simulated by GMI  
5 CTM driven by three meteorological datasets (1995 for fvGCM, 2005 for GEOS4 and MERRA).



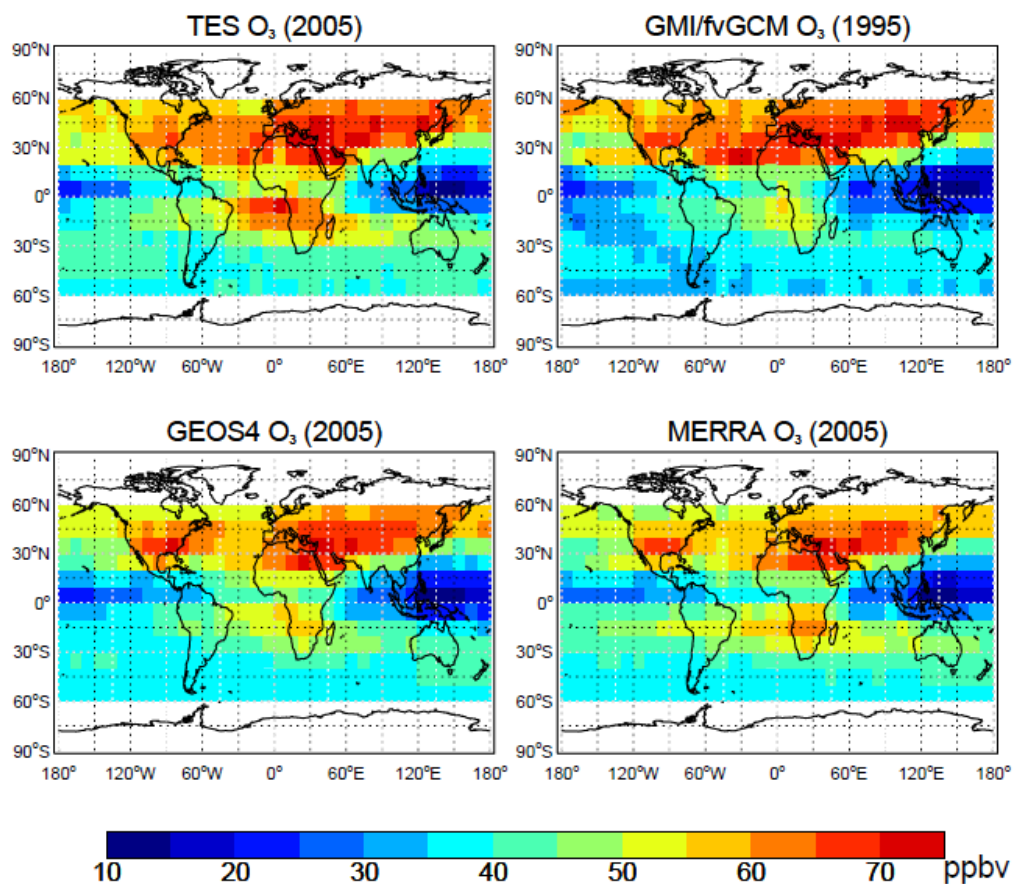
1  
2  
3  
4  
5

**Figure 9.** Mean  $^{222}\text{Rn}$  concentrations ( $\text{mBq SCM}^{-1}$ ) (left column), stratospheric fraction (%) of tropospheric  $^7\text{Be}$  concentrations (middle column), and ratios of  $^7\text{Be}$  to  $^{210}\text{Pb}$  volume mixing ratios (right column) at 618 hPa in the GMI model driven by the fvGCM (1995), GEOS4 (2005), and MERRA (2005) meteorological data sets for the period of July - August.



1

2



3

4

5

6

7

8

9

**Figure 10.** Mean mixing ratios of O<sub>3</sub> at 618 hPa observed by TES during July- August 2005 and corresponding GMI CTM results with 3-hourly output sampled along the TES orbit tracks. TES averaging kernels and *a priori* were applied to the model output. Results are averaged into 10°×10° grid cells.

10

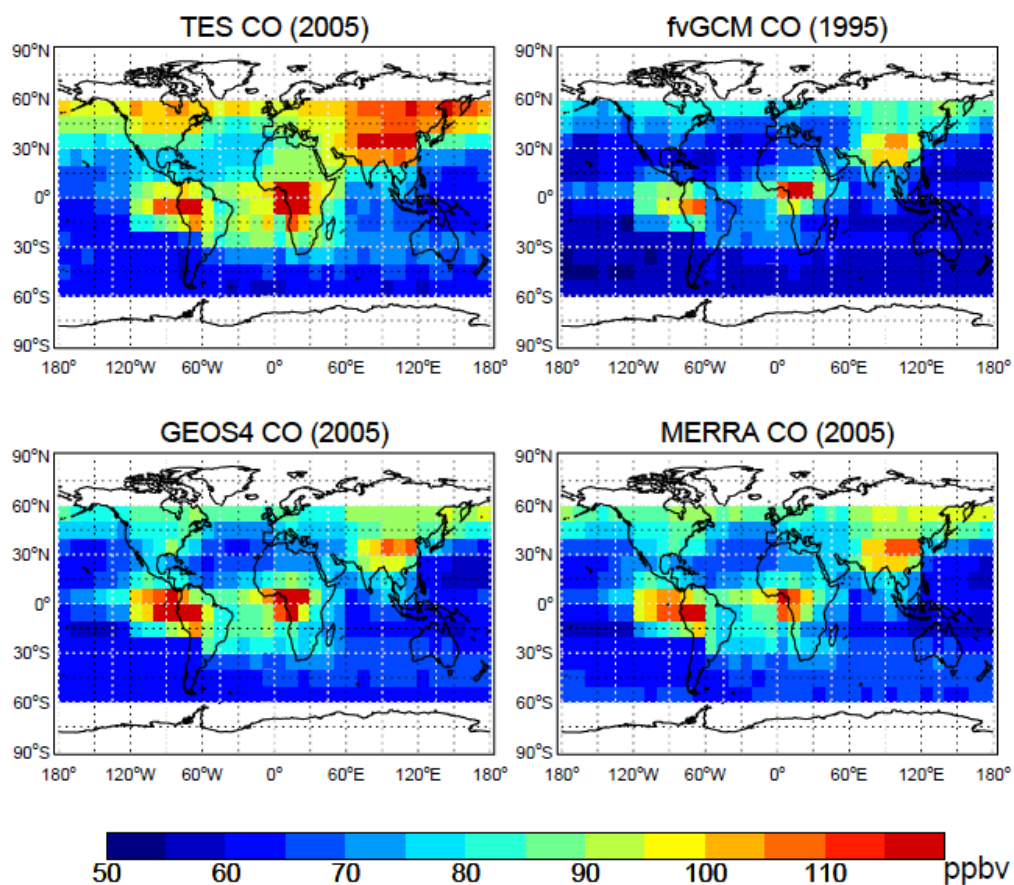
11

12

13

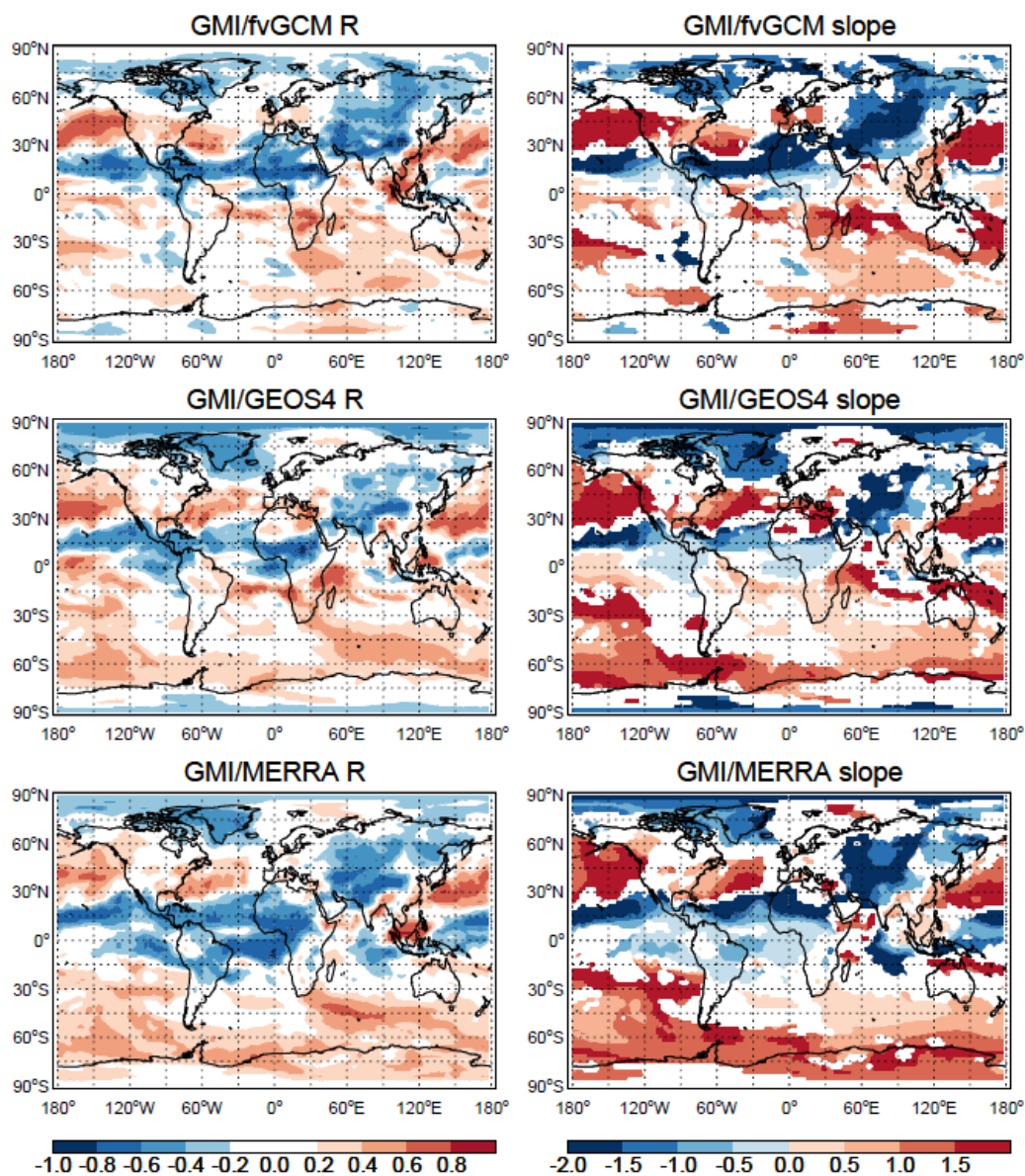


1  
2  
3

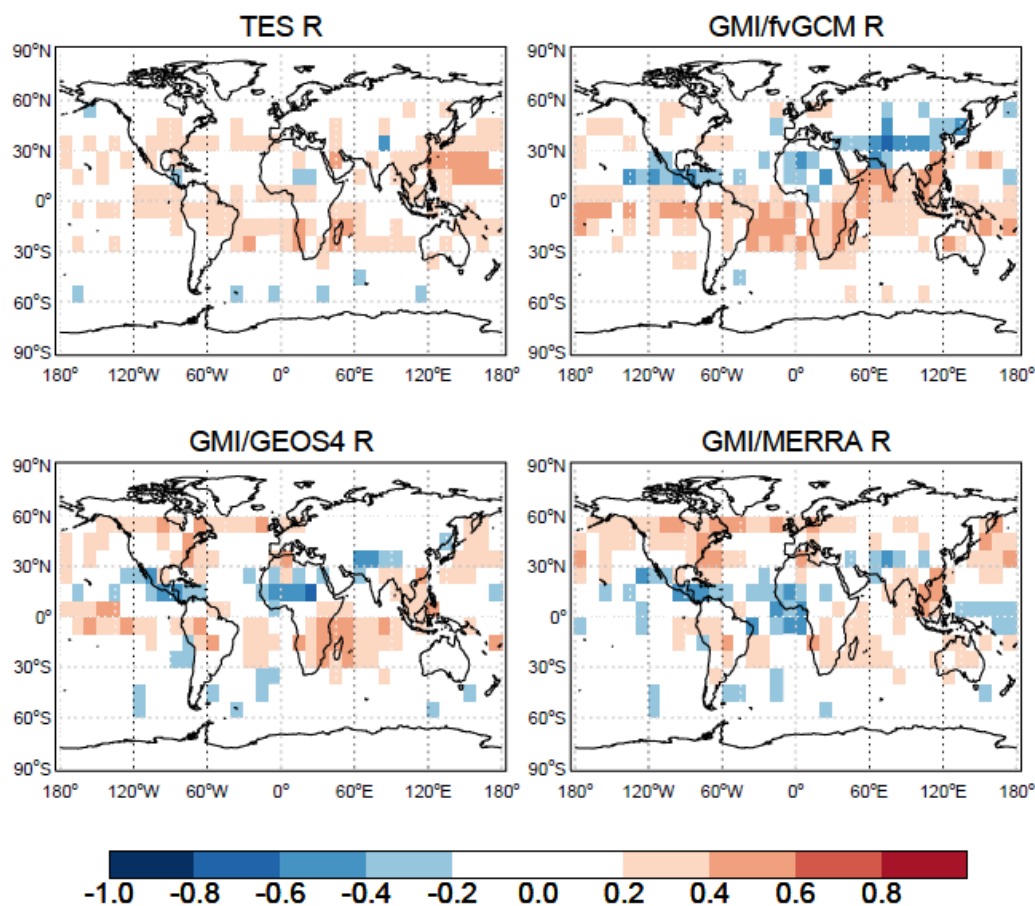


4  
5  
6  
7  
8

Figure 11. Same as Figure 10, but for CO.

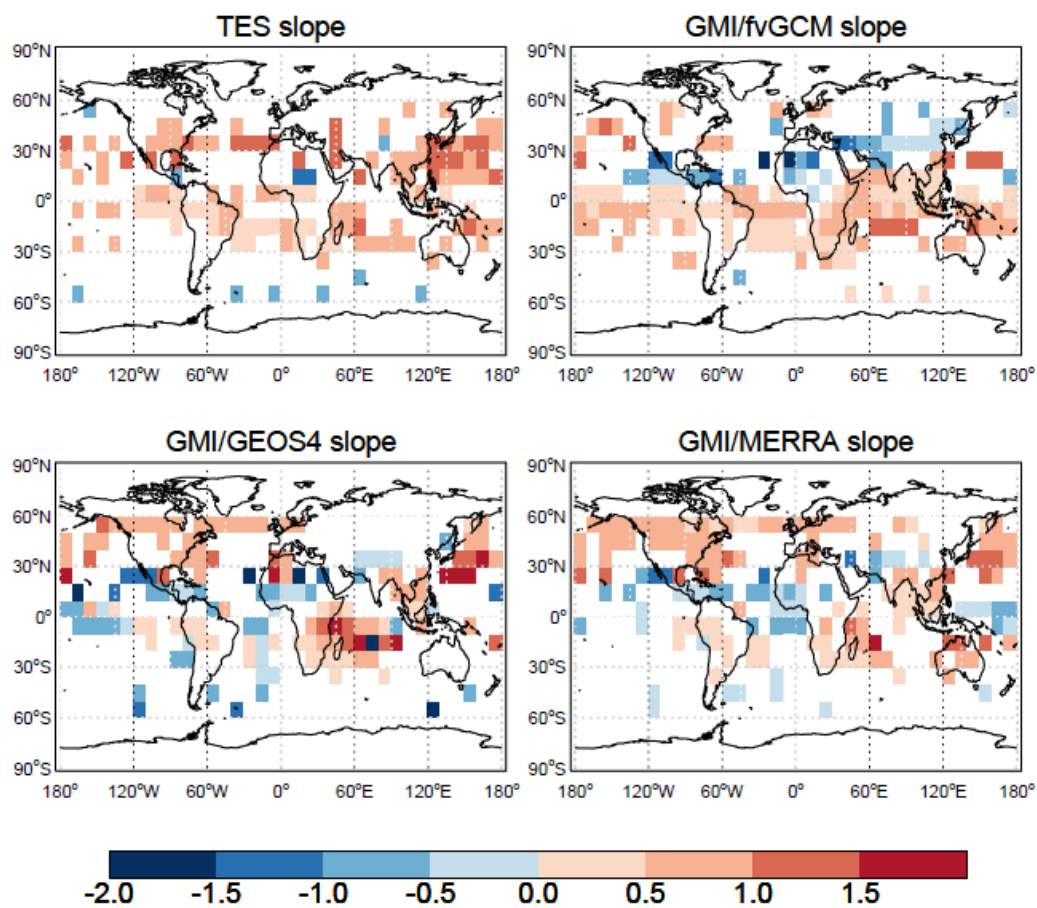


3 **Figure 12.** O<sub>3</sub>-CO correlation coefficients (R) and linear regression slopes (dO<sub>3</sub>/dCO) at 618 hPa  
4 in the GMI model driven by the fvGCM (1995), GEOS4 (2005), and MERRA (2005)  
5 meteorological fields. Results are calculated in 2°×2.5° grid cells using 3-hourly model output  
6 and the reduced major axis method. White areas denote absolute values of O<sub>3</sub>-CO correlation  
7 coefficients less than 0.2.



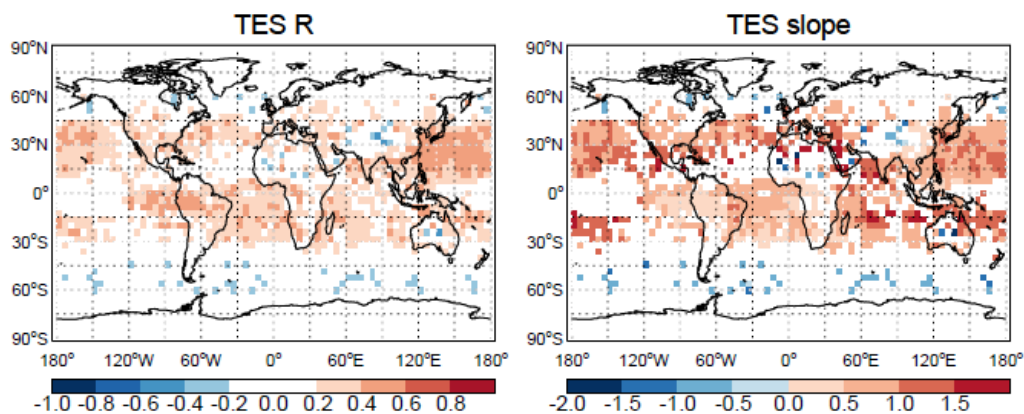
1  
2  
3

4 **Figure 13.** O<sub>3</sub>-CO correlation coefficients (R) at 618 hPa as determined by O<sub>3</sub> and CO observations  
5 from TES during July – August 2005, and corresponding GMI CTM results with 3-hourly output  
6 sampled along the TES orbit tracks. TES averaging kernels, spectral errors, and a priori are applied.  
7 Results are calculated in 10°×10° grid cells. White areas denote absolute values of O<sub>3</sub>-CO  
8 correlation coefficients less than 0.2.



1  
2  
3  
4  
5  
6

**Figure 14.** Same as **Figure 13**, but for linear regression slopes  $dO_3/dCO$ .



1  
2  
3  
4  
5  
6  
7  
8

**Figure 15.** O<sub>3</sub>-CO correlation coefficients (R) and linear regression slopes (dO<sub>3</sub>/dCO) at 618 hPa as determined by O<sub>3</sub> and CO observations from TES during July–August, 2005 – 2009. Results are calculated in 4°×5° grid cells. White areas denote absolute values of O<sub>3</sub>-CO correlation coefficients less than 0.2.

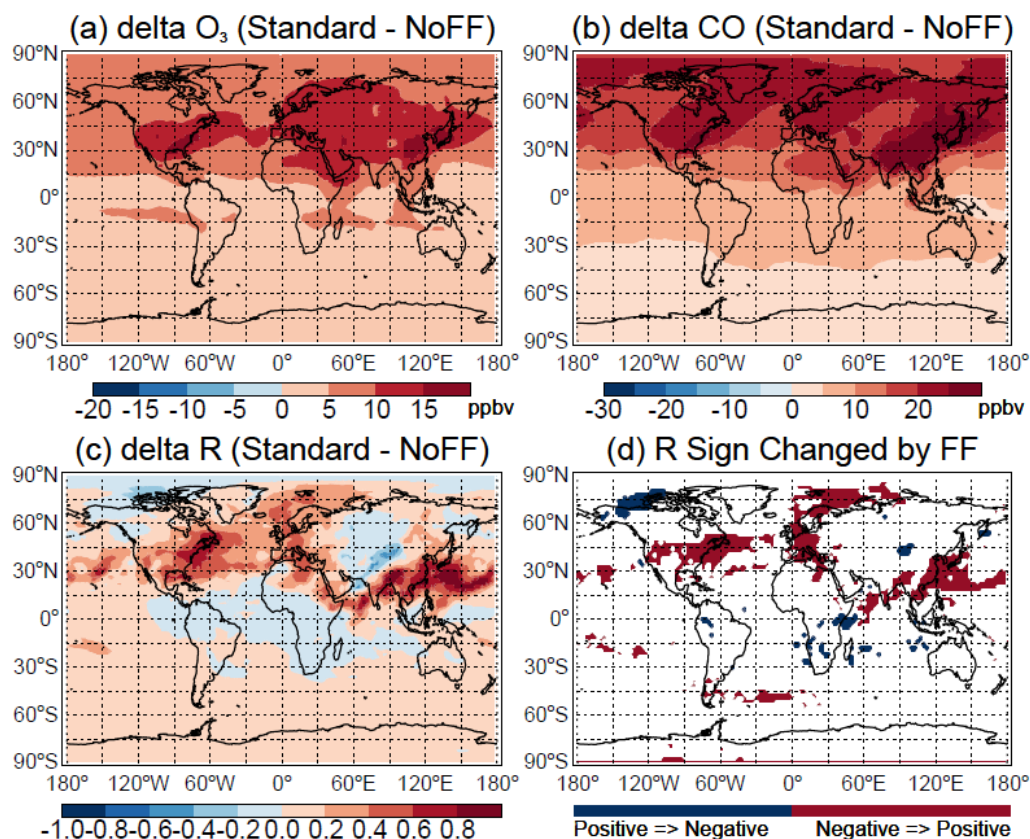


**Figure 16.** Sensitivity of  $O_3$ , CO, and their correlations to fossil fuel (FF) emissions during July – August 2005. The plots show the mean differences in (a)  $O_3$ , (b) CO mixing ratios (ppbv), and (c)  $O_3$ -CO correlation coefficients (R) at 618 hPa between the standard GMI/MERRA simulation and a simulation where fossil fuel emissions are suppressed (NoFF) in the model. Also shown in (d) are the areas with changed correlation signs. Results are calculated using 3-hourly model output.

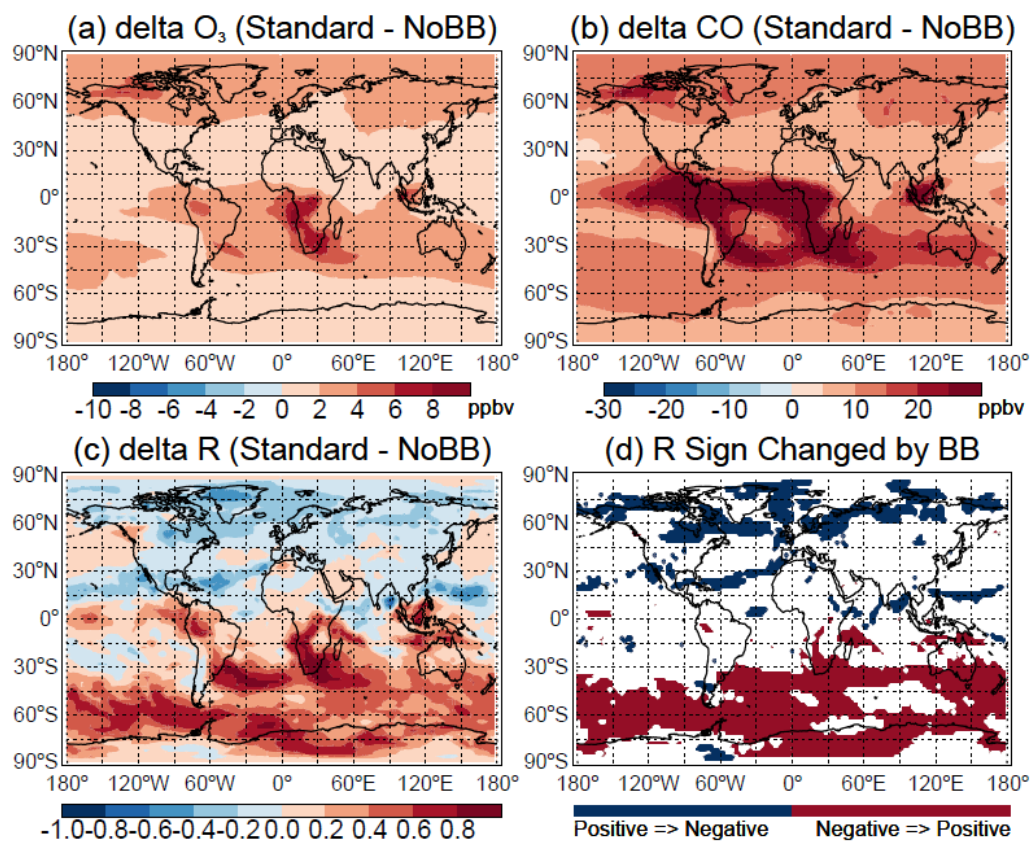
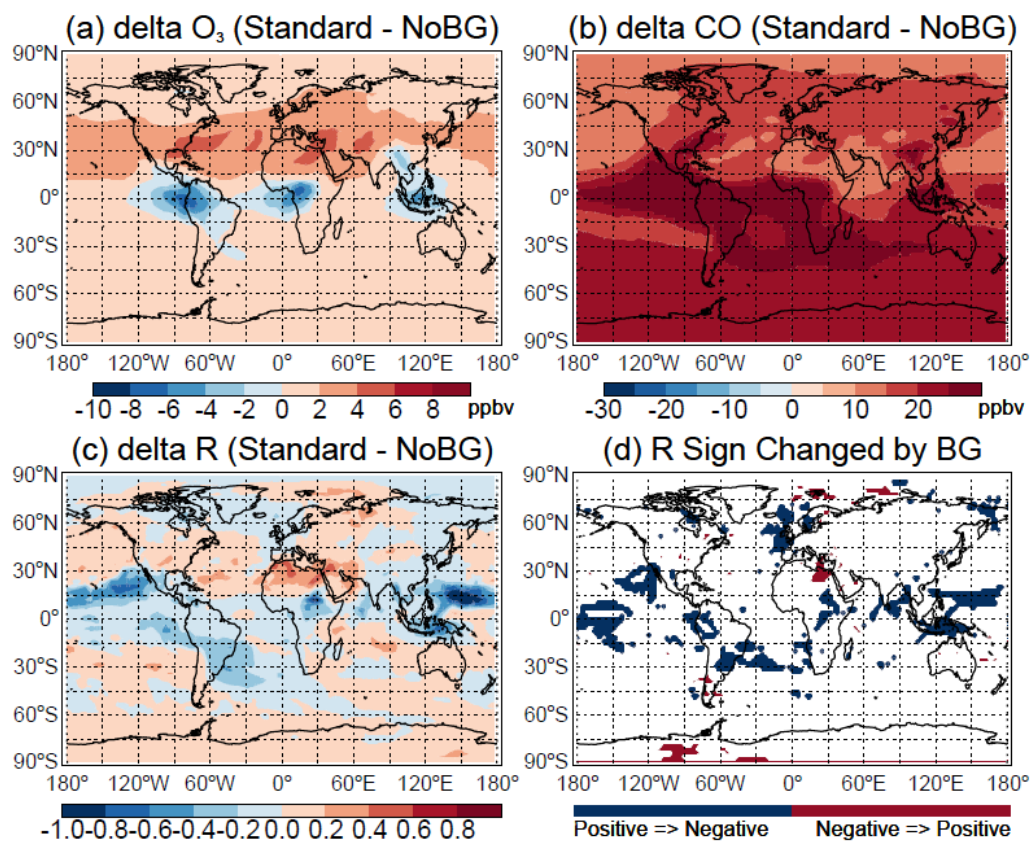


**Figure 17.** Same as **Figure 16**, but for the sensitivity of O<sub>3</sub>, CO, and their correlations at 618 hPa to biomass burning (BB) emissions.



1  
2  
3  
4  
5  
6

**Figure 18.** Same as **Figure 16**, but for the sensitivity of  $O_3$ , CO, and their correlations at 618 hPa to biogenic (BG) emissions.

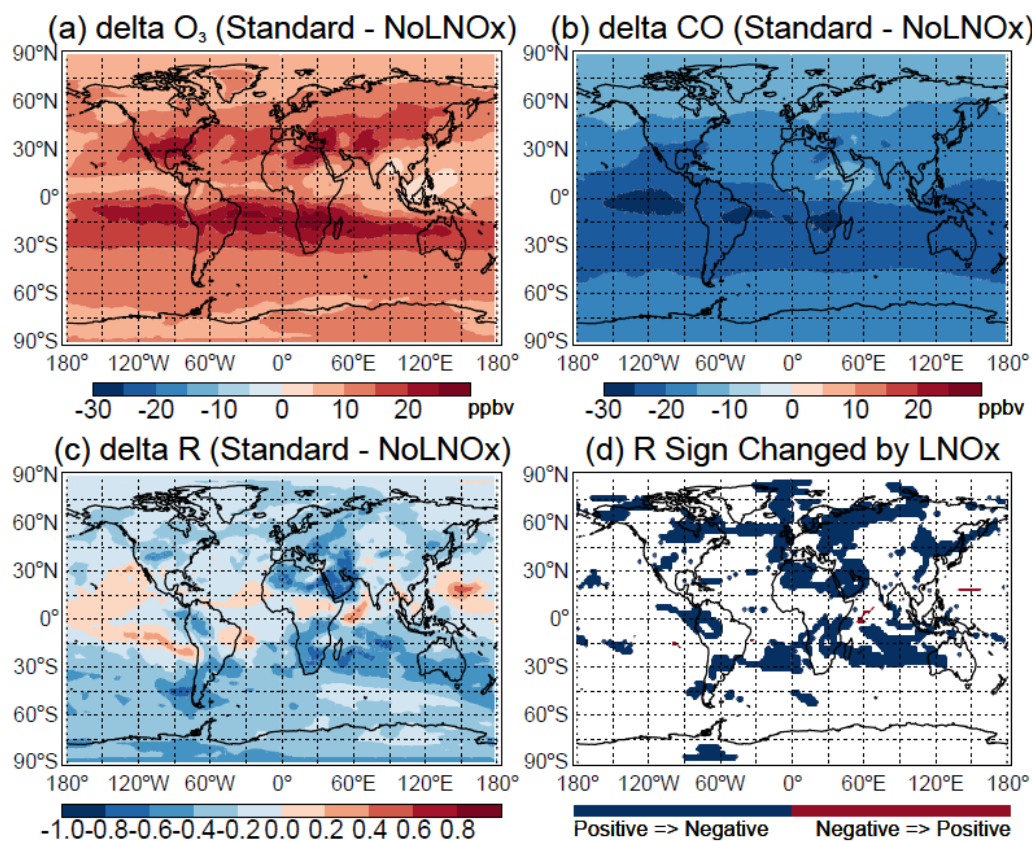
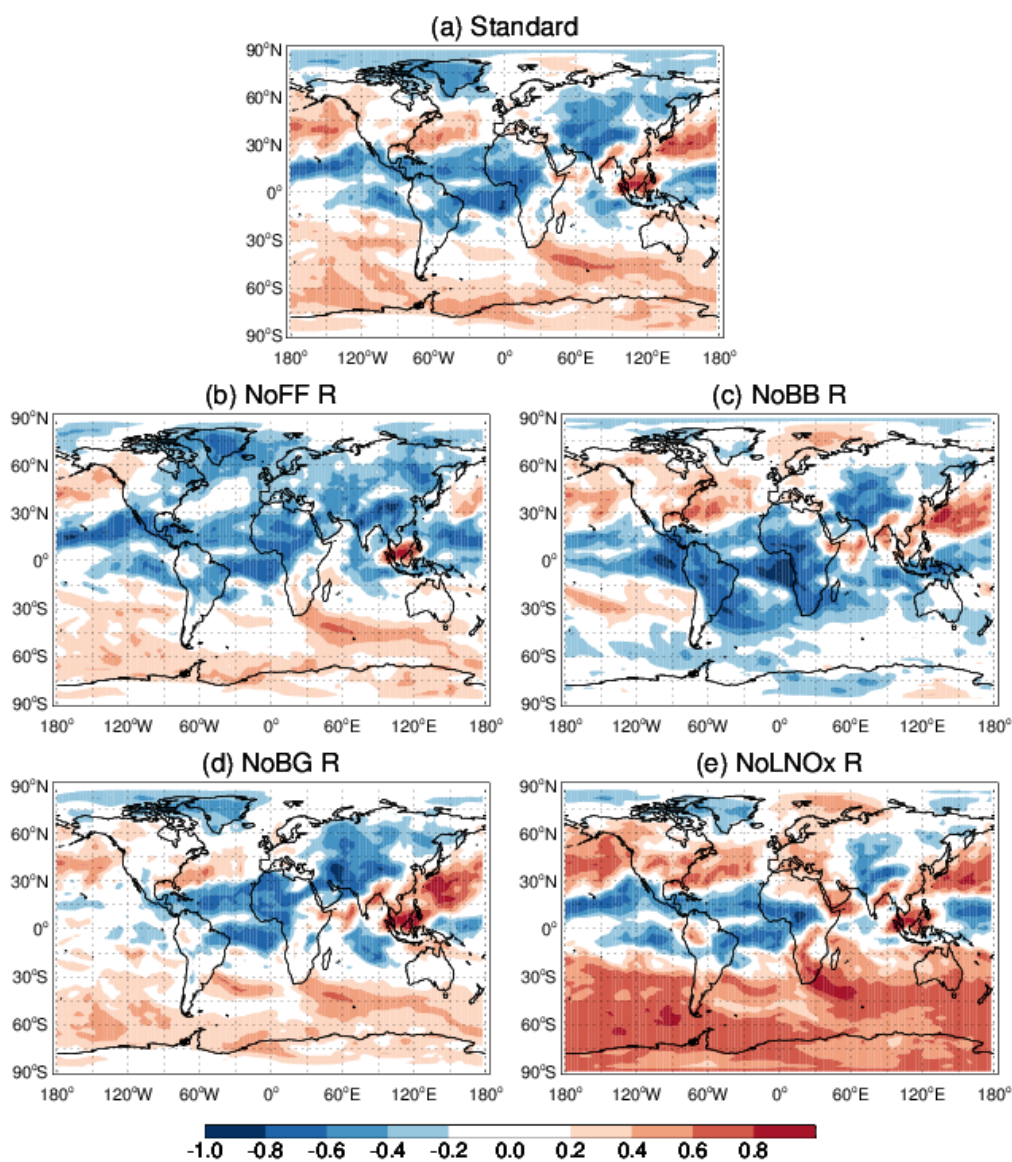


**Figure 19.** Same as **Figure 16**, but for the sensitivity of O<sub>3</sub>, CO, and their correlations at 618 hPa to lightning NO<sub>x</sub> (LNO<sub>x</sub>) emissions.



1

2

3 **Figure 20.** GMI/MERRA-simulated O<sub>3</sub>-CO correlations (R) at 618 hPa (a) in the standard  
4 simulation and (b) - (e) when fossil fuel (FF), biomass burning (BB), biogenic (BG), and lightning  
5 NO<sub>x</sub> (LNO<sub>x</sub>) emissions are individually suppressed (NoFF, NoBB, NoBG, and NoLNO<sub>x</sub>,  
6 respectively) in the model during July-August 2005. Results are calculated using 3-hourly model  
7 output. White areas denote absolute values of O<sub>3</sub>-CO correlation coefficients less than 0.2.